J. Fluid Mech. (1989), *vol.* 207, *pp.* 191–229
Printed in Great Britain

The shearless turbulence mixing layer

By S. VEERAVALLI AND Z. WARHAFT
Sibley School of Mechanical and Aerospace Engineering, Cornell University,
Ithaca, NY 14853, USA

(Received 8 November 1988 and in revised form 13 March 1989)

The interaction of two energy-containing turbulence scales is studied in the absence of mean shear. The flow, a turbulence mixing layer, is formed in decaying grid turbulence in which there are two distinct scales, one on either side of the stream. This is achieved using a composite grid with a larger mesh spacing on one side of the grid than the other. The solidity of the grid, and thus the mean velocity, is kept constant across the entire flow. Since there is no mean shear there is no turbulence production and thus spreading is caused solely by the fluctuating pressure and velocity fields. Two different types of grids were used: a parallel bar grid and a perforated plate. The mesh spacing ratio was varied from 3.3:1 to 8.9:1 for the bar grid, producing a turbulence lengthscale ratio of 2.4:1 and 4.3:1 for two different experiments. For the perforated plate the mesh ratio was 3:1 producing a turbulence lengthscale ratio of 2.2:1. Cross-stream profiles of the velocity variance and spectra indicate that for the large lengthscale ratio (4.3:1) experiment, a single scale dominates the flow while for the smaller lengthscale ratio experiments, the energetics are controlled by both lengthscales on either side of the flow. In all cases the mixing layer is strongly intermittent and the transverse velocity fluctuations have large skewness. The downstream data of the second, third and fourth moments for all experiments collapse well using a single composite lengthscale. The component turbulent energy budgets show the importance of the triple moment transport and pressure terms within the layer and the dominance of advection and dissipation on the outer edge. It is also shown that the bar grids tend toward self-similarity with downstream distance. The perforated plate could not be measured to the same downstream extent and did not reach self-similarity within its measurement range. In other respects the two types of grids yielded qualitatively similar results. Finally, we emphasize the distinction between intermittent turbulent penetration and turbulent diffusion and show that both play an important role in the spreading of the mixing layer.

1. Introduction

Fully developed turbulence consists of a complex continuous spectrum of interacting scales. Although the interaction of the various spectral modes is still poorly understood (see for example Herring 1985), success in modelling the gross characteristics of simple turbulent flows such as wakes, jets and mixing layers, has been achieved by recognizing that there is a single dominant energy-containing scale for these cases. Thus the spreading rate and energetics of the above-mentioned free-shear flows are well predicted (Tennekes & Lumley 1972). However, many turbulent flows have more than one dominant scale, for example a turbulent boundary layer developing in free-stream turbulence, and these flows are difficult to model or

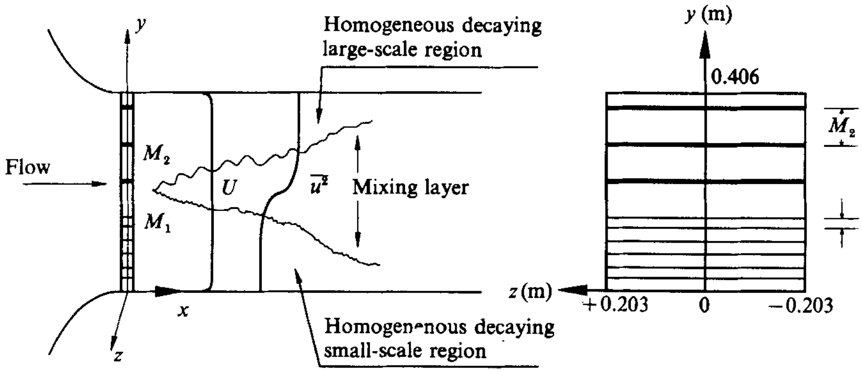

FIGURE 1. Sketch of the wind tunnel showing the grid consisting of the two different mesh lengths. $M_1 < M_2$. Also shown are typical mean (U) and longitudinal variance ($\overline{u^2}$) profiles and the coordinate system used. The actual grid designs are shown in figures 2 and 3 below.

predict† without a detailed understanding of the spectral dynamics. Simple superposition fails because of the nonlinearity of the interactions. It is towards gaining a better understanding of the interaction of two dominant energy-containing scales that the experiment to be described here was conducted.

The flow, a shearless turbulence mixing layer, is formed in decaying grid turbulence in which the mean velocity is constant throughout, but two distinct scales of turbulence are formed on either side of the stream (figure 1). As the flow evolves these two different turbulent fields penetrate and diffuse into one another. This flow, free of complex turbulent shear production mechanisms, relies for its evolution solely on turbulence–turbulence interactions. (The governing equations are discussed in §2). For this reason we have called it a *turbulence* (rather than *turbulent*) mixing layer. In this regard, it seems to be more fundamental than the traditional turbulent mixing layer formed because of an instability between two parallel streams each moving at a different speed, a flow that has been extensively studied in the past (Townsend 1976; Breidenthal 1981). Surprisingly, the shearless turbulence mixing layer has received little attention. Apart from our preliminary study (Veeravalli & Warhaft 1987, hereinafter referred to as V&W) the only previous experiment appears to be due to Gilbert (1980) but because of his flow configuration he failed to observe the large-scale intermittency in the mixing layer, perhaps the most important and unusual characteristic of this flow which is homogeneous in the mean. Gilbert's work will be discussed in relation to our own results below.

The shearless mixing layer is very difficult to set up experimentally. In V&W we devoted most of the paper to problems associated with attaining the prescribed flow. These problems will be discussed further in §3 below. We also described some preliminary results pertaining to the evolution of the mixing layer for a parallel bar grid with a single mesh length ratio (see §3 for a description of the grids). In the present study the mesh length ratio (and hence the ratio of the dominant scale sizes) for the parallel bar grid is varied and a new way of generating the mixing layer by means of a perforated plate is described. Thus here we are particularly concerned with how varying initial conditions affects the evolution of the flow. We also study the energy budgets and spectra; these were not documented by V&W. Furthermore,

---

† For instance, Rodi & Scheuerer (1985) show that the dependence of the interaction between boundary layer and free-stream turbulence on the free-stream lengthscale, predicted by k–ϵ and second-order models, is opposite to what is observed experimentally.

since our previous study, we have devised new ways to tune the flow and thus we believe the results presented here are more representative of the ideal than those presented in V&W, although both sets are in qualitative agreement.

Finally, our study in some ways springs from our earlier work concerning passive scalars (Warhaft 1981, 1984; Sirivat & Warhaft 1983). In those experiments we were interested in the interaction of more than one scalar field, each with its own dominant scale and spectrum. Of course linear super-position must hold for passive scalar fields but not for the velocity field. Indeed the present study shows that the interaction of two velocity fields is much more complex to set up experimentally and it is also harder to draw general inferences from it.

2. The governing equations

The objective of this investigation was to study the interaction of two distinct turbulent scales in the absence of mean shear. A composite grid of two different mesh sizes but with a constant pressure drop was used to generate the flow. Since the pressure drop is constant, the amount of energy transferred from the mean motion to turbulent fluctuations at the grid is the same across the whole flow. However, because of the smaller scales, the initial decay is much faster on the small-mesh side of the flow (Batchelor 1953). Thus, when both regions enter the power-law decay regime, at about 20 mesh lengths from the grid (Hinze 1975), both the turbulence intensity and the lengthscale are larger on the large-mesh side than on the small-mesh side. (The power-law decay of the turbulent energy and its components is documented below, see §3, table 1.) However, the decay exponent is approximately the same on both sides of the mixing layer because the grid geometry is the same. Hence, the energy and scale ratios remain constant with downstream distance. The salient features of the flow then are (figure 1): the only mean velocity component is U; there are no mean velocity gradients; the flow is strongly inhomogeneous in the y-direction, decaying and weakly developing in the x-direction and homogeneous in the z-direction. Thus the evolution equations for the velocity variances are†

$$U\frac{\partial}{\partial x}(\overline{u^2})+\frac{\partial}{\partial x}(\overline{u^3})+\frac{\partial}{\partial y}(\overline{u^2v}) = \frac{2}{\rho}\overline{p\frac{\partial u}{\partial x}}-\frac{2}{\rho}\frac{\partial}{\partial x}(\overline{pu})-2\nu\left(\overline{\frac{\partial u}{\partial x_j}\frac{\partial u}{\partial x_j}}\right), \tag{1a}$$

$$U\frac{\partial}{\partial u}(\overline{v^2})+\frac{\partial}{\partial x}(\overline{uv^2})+\frac{\partial}{\partial y}(\overline{v^3}) = \frac{2}{\rho}\overline{p\frac{\partial v}{\partial y}}-\frac{2}{\rho}\frac{\partial}{\partial y}(\overline{pv})-2\nu\left(\overline{\frac{\partial v}{\partial x_j}\frac{\partial v}{\partial x_j}}\right), \tag{1b}$$

$$U\frac{\partial}{\partial x}(\overline{w^2})+\frac{\partial}{\partial x}(\overline{uw^2})+\frac{\partial}{\partial y}(\overline{vw^2}) = \frac{2}{\rho}\overline{p\frac{\partial w}{\partial z}}-2\nu\left(\overline{\frac{\partial w}{\partial x_j}\frac{\partial w}{\partial x_j}}\right), \tag{1c}$$

where, as usual, upper case letters denote mean quantities and lower case letters represent fluctuations. The overbars denote average values, p is the pressure fluctuation and ν and ρ are the kinematic viscosity and density respectively (both are constant). The kinetic energy equation may be obtained by summing one half of (1 *a*), (1 *b*) and (1 *c*) and is

$$U\frac{\partial k}{\partial x}+\frac{\partial}{\partial x}\left(\overline{\frac{u(u^2+v^2+w^2)}{2}}\right)+\frac{\partial}{\partial y}\left(\overline{\frac{v(u^2+v^2+w^2)}{2}}\right) = -\frac{1}{\rho}\frac{\partial}{\partial y}(\overline{pv})-\frac{1}{\rho}\frac{\partial}{\partial x}(\overline{pu})-\nu\overline{\frac{\partial u_i}{\partial x_j}\frac{\partial u_i}{\partial x_j}}, \tag{2}$$

where, $k \equiv \frac{1}{2}(\overline{u^2}+\overline{v^2}+\overline{w^2})$.

---

† The notation $\boldsymbol{x} = (x, y, z)$ and $\boldsymbol{u} = (u, v, w)$ will be used interchangeably with $\boldsymbol{x} = (x_1, x_2, x_3)$ and $\boldsymbol{u} = u_1, u_2, u_3)$.

In the equations above, the downstream transport terms (second term on the left-hand side of (1*a*), (1*b*), (1*c*) and (2) and the second term on the right-hand side of (1*a*) and (2)) should be negligible as the flow is slowly developing with x. However, they have been included to emphasize the form of the equations. The equations show the absence of production and indicate a balance between the advection, dissipation, triple-correlation transport and pressure transport and scrambling terms (the scrambling term is not present in the total kinetic energy budget). Since the turbulence is decaying across the whole flow, we would expect dissipation to contribute significantly to the budget in all regions. This should be compared with the behaviour in free shear flows where the dissipation is negligible at the outer edge of the flow and advection balances transport (Townsend 1976).

In shear flows, the mean velocity gradients give rise to the off-diagonal Reynolds stresses; the absence of mean velocity gradients here would suggest that these stresses should be zero. However, in this flow there is another mechanism by which $\overline{uv}$ may be generated, as was earlier noted in V&W. The z-component of the curl of the mean momentum equation is

$$\frac{\partial}{\partial y}\frac{\partial}{\partial x}(\overline{u^2}-\overline{v^2}) = \frac{\partial^2}{\partial x^2}(\overline{uv})-\frac{\partial^2}{\partial y^2}(\overline{uv}). \tag{3}$$

Even for homogeneous 'isotropic' grid turbulence $\overline{u^2} \neq \overline{v^2}$ (Comte-Bellot & Corrsin 1966) and within the mixing layer, (1*a*) and (1*b*) indicate different behaviours for $\overline{u^2}$ and $\overline{v^2}$. Furthermore, the turbulence is decaying and the mixing layer is thickening and thus the left-hand side of (3) should not be zero. Therefore $\overline{uv}$ cannot be identically zero in the mixing layer. Indeed, in §3 we shall show that a small but significant value of $\overline{uv}$ does occur because of the above mechanism, and while it does not influence the kinetic energy budget, it does give rise to a production term in the $\overline{u^3}$ equation. The budget for $\overline{uv}$ is

$$\underbrace{U\frac{\partial \overline{uv}}{\partial x}}_{\text{(advection)}}+\underbrace{\frac{\partial}{\partial y}\left\{\overline{uv^2}+\frac{1}{\rho}\overline{up}\right\}}_{\text{(transport)}} = \underbrace{\frac{1}{\rho}\left[\overline{p\left[\frac{\partial u}{\partial y}+\frac{\partial v}{\partial x}\right]}\right]}_{\text{(pressure effects)}}. \tag{4}$$

The dynamics of the second-order mixing layer are further elucidated by a study of the third-order and fourth-order moments. The transport equations for the third-order terms of relevance are

$$\underbrace{U\frac{\partial}{\partial x}\frac{\overline{u^3}}{3}}_{\text{(advection)}}+\underbrace{\frac{\partial}{\partial y}\left[\frac{\overline{u^3v}}{3}-\overline{u^2}\,\overline{uv}\right]}_{\text{(transport)}}+\underbrace{\overline{uv}\frac{\partial}{\partial y}\overline{u^2}}_{\text{(production)}} = \underbrace{+\frac{1}{\rho}\overline{p\frac{\partial u^2}{\partial x}}}_{\text{(pressure effects)}}+\underbrace{\overline{\nu u^2\frac{\partial^2 u}{\partial x_j\,\partial x_j}}}_{\text{(viscous effects)}}, \tag{5a}$$

$$\underbrace{U\frac{\partial}{\partial x}\frac{\overline{v^3}}{3}}_{\text{(advection)}}+\underbrace{\frac{\partial}{\partial y}\frac{\overline{v^4}}{3}}_{\text{(transport)}}-\underbrace{\overline{v^2}\frac{\partial}{\partial y}\overline{v^2}}_{\text{(production)}} = \underbrace{-\frac{1}{\rho}\frac{\partial}{\partial y}\overline{pv^2}}_{\text{(transport)}}+\underbrace{\frac{1}{\rho}\overline{p\frac{\partial v^2}{\partial y}}}_{\text{(pressure effects)}}+\underbrace{\overline{\nu v^2\frac{\partial^2 v}{\partial x_j\,\partial x_j}}}_{\text{(viscous effects)}}, \tag{5b}$$

$$\begin{aligned}&\underbrace{U\frac{\partial}{\partial x}\overline{u^2v}}_{\text{(advection)}}+\underbrace{\frac{\partial}{\partial y}\overline{u^2v^2}}_{\text{(transport)}}\underbrace{-2\,\overline{uv}\frac{\partial}{\partial y}\overline{uv}-\overline{u^2}\frac{\partial}{\partial y}\overline{v^2}}_{\text{(production)}}\\ &\quad= \underbrace{-\frac{1}{\rho}\frac{\partial}{\partial y}\overline{pu^2}}_{\text{(transport)}}+\underbrace{\frac{1}{\rho}\left[\overline{2p\frac{\partial uv}{\partial x}}+\overline{p\frac{\partial u^2}{\partial y}}\right]}_{\text{(pressure effects)}}+\underbrace{\nu\left[\overline{2uv\frac{\partial^2 u}{\partial x_j\,\partial x_j}}+\overline{u^2\frac{\partial^2 v}{\partial x_j\,\partial x_j}}\right]}_{\text{(viscous effects)}},\end{aligned} \tag{5c}$$

and

$$\underset{\text{(advection)}}{U\frac{\partial}{\partial x}\overline{w^2v}}+\underset{\text{(transport)}}{\frac{\partial}{\partial y}\overline{w^2v^2}}-\underset{\text{(production)}}{\overline{w^2}\frac{\partial}{\partial y}\overline{v^2}}$$

$$=\underset{\text{(transport)}}{-\frac{1}{\rho}\left[\frac{\partial}{\partial y}\overline{pw^2}\right]}+\underset{\text{(pressure effects)}}{\frac{1}{\rho}\left[\overline{2p\frac{\partial vw}{\partial z}}+\overline{p\frac{\partial w^2}{\partial y}}\right]}+\underset{\text{(viscous effects)}}{\nu\left[\overline{2wv\frac{\partial^2 w}{\partial x_j\,\partial xj}}+\overline{w^2\frac{\partial^2 v}{\partial x_j\,\partial x_j}}\right]}. \qquad (5d)$$

(All the terms in the $\overline{w^3}$ equation are zero by symmetry.) Similarly, the equations for $\overline{u^4}$, $\overline{u^4}$ and $\overline{w^4}$ are:

$$\underset{\text{(advection)}}{U\frac{\partial}{\partial x}\frac{\overline{u^4}}{4}}+\underset{\text{(transport)}}{\frac{\partial}{\partial y}\frac{\overline{u^4v}}{4}}-\underset{\text{(production)}}{\overline{u^3}\frac{\partial\overline{uv}}{\partial y}}=\underset{\text{(pressure effects)}}{+\frac{1}{\rho}\overline{p\frac{\partial u^3}{\partial x}}}+\underset{\text{(viscous effects)}}{\nu\overline{u^3\frac{\partial^2 u}{\partial x_j\,\partial x_j}}}, \qquad (6a)$$

$$\underset{\text{(advection)}}{U\frac{\partial}{\partial x}\frac{\overline{v^4}}{4}}+\underset{\text{(transport)}}{\frac{\partial}{\partial y}\frac{\overline{v^5}}{4}}-\underset{\text{(production)}}{\overline{v^3}\frac{\partial}{\partial y}\overline{v^2}}=\underset{\text{(transport)}}{-\frac{1}{\rho}\frac{\partial}{\partial y}\overline{pv^3}}+\underset{\text{(pressure effects)}}{\frac{1}{\rho}\overline{p\frac{\partial v^3}{\partial y}}}+\underset{\text{(viscous effects)}}{\nu\overline{v^3\frac{\partial^2 v}{\partial x_j\,\partial x_j}}}, \qquad (6b)$$

$$\underset{\text{(advection)}}{U\frac{\partial}{\partial x}\frac{\overline{w^4}}{4}}+\underset{\text{(transport)}}{\frac{\partial}{\partial y}\frac{\overline{w^4v}}{4}}=\underset{\text{(pressure effects)}}{\frac{1}{\rho}\overline{p\frac{\partial w^3}{\partial z}}}+\underset{\text{(viscous effects)}}{\nu\overline{w^3\frac{\partial^2 w}{\partial x_j\,\partial x_j}}}. \qquad (6c)$$

Just as the gradients of the mean velocity components give rise to the production term in the equations for the second-order quantities, gradients of second-order moments generate production terms in the third and fourth moment equations. We note that the pressure and velocity correlation transport terms in (5*b*), (5*c*) and (5*d*) arise from lateral gradients of quantities containing even powers of the velocity field; namely, $\overline{v^4}$, $\overline{u^2v^2}$, $\overline{w^2v^2}$, $\overline{pv^2}$, $\overline{pu^2}$ and $\overline{pw^2}$. These even moments need not be zero in the two homogeneous edges of the mixing layer and in general will have different values in the large- and small-scale homogeneous regions. Hence, in these equations, there is a net flux from the homogeneous region at $y \rightarrow +\infty$ to $y \rightarrow -\infty$. This effect is not present in the equations for $\overline{u^4}$, $\overline{v^4}$ and $\overline{w^4}$ since in these equations (as in the variance equations), the transport terms arise from gradients of odd moments of the velocity field. We also note that the terms labelled pressure effects in (5) and (6) are more complex in nature than the corresponding redistribution term in the variance equations.

The above equations will be further discussed with reference to our data on third and fourth moments (§4.3).

3. Experimental apparatus and method of flow realization

The experiments were conducted in a vertically oriented wind tunnel (Sirivat & Warhaft 1983) with a test section 4.25 m long and a cross-section of 0.406×0.406 m^2. Figure 1 shows a schematic view of the tunnel and the coordinate system used. Henceforth, quantities (such as the mesh size M, lengthscale l, velocity variance $\overline{u^2}$, etc.), with the subscript 1, characterize the low-turbulence homogeneous region and those with the subscript 2 characterize the high-turbulence homogeneous region of the flow. Three grids were used; two parallel bar grids ($M_2/M_1 = 3.3$, $M_2/M_1 = 8.9$) and a perforated plate ($M_2/M_1 = 3$)†. The values of the mesh sizes, M_1 and M_2 and the

---

† Formally, the term 'grid' refers to a crossed-bar structure. However, we call the parallel bar arrays and the perforated plate used here grids, because they produce grid turbulence; i.e. they produce turbulence that is qualitatively very similar to that of traditional biplanar crossed-bar grids.

Flow parameters	3.3:1 Parallel bar grid	8.9:1 Parallel bar grid	3:1 Perforated plate
M_1(cm)	0.95	0.477	1.12
M_2 (cm)	3.15	4.25	3.35
solidity σ	0.32	0.29	0.31
location of the geometric centre (cm)	18.24	14.4	20.04
mean velocity U(m/s)	5.9	5.85	5.8
$R_{M_1} \equiv UM_1/\nu$	3505	1744	4060
$R_{M_2} \equiv UM_2/\nu$	11616	15539	12180
$k_1 \equiv \frac{1}{2}(\overline{u_1^2}+\overline{v_1^2}+\overline{w_1^2})$ (m^2/s^2)	0.0134	0.0058	0.00815
$\epsilon_1 = -\mathrm{d}k_1/\mathrm{d}t$ (m^2/s^3)	0.103	0.045	0.090
$l_1 \equiv k_1^{\frac{3}{2}}/\epsilon_1$ (cm)	1.49	0.98	0.80
$k_2 \equiv \frac{1}{2}(\overline{u_2^2}+\overline{v_2^2}+\overline{w_2^2}$ (m^2/s^2)	0.083	0.134	0.051
$\epsilon_2 = -\mathrm{d}k_2/\mathrm{d}t$ (m^2/s^3)	0.641	1.16	0.655
$l_2 = k_2^{\frac{3}{2}}/\epsilon$(cm)	3.60	4.23	1.78
$\lambda_1 \equiv (\overline{u_1^2})^{\frac{1}{2}}/(\epsilon_1/15\nu)^{\frac{1}{2}}$ (cm)	0.48	0.46	0.42
$\lambda_2 \equiv (\overline{u_2^2})^{\frac{1}{2}}/(\epsilon_2/15\nu)^{\frac{1}{2}}$ (cm)	0.49	0.47	0.37
$R_{l_1} \equiv l_1(\overline{u_1^2})^{\frac{1}{2}}/\nu$	92.6	38.8	40.3
$R_{l_2} \equiv l_2(\overline{u_2^2})^{\frac{1}{2}}/\nu$	573.6	868.8	214
$R_{\lambda_1} \equiv \lambda_1(\overline{u_1^2})^{\frac{1}{2}}/\nu$	29.8	18.2	21.2
$R_{\lambda_2} \equiv \lambda_2(\overline{u_2^2})^{\frac{1}{2}}/\nu$	78.1	96.5	44.5
$\tau_1 \equiv k_1/\epsilon_1$ (s)	0.130	0.129	0.091
$\tau_2 \equiv k_2/\epsilon_2$ (s)	0.129	0.116	0.078
τ_1/τ_2	1.01	1.12	1.17
l_2/l_1	2.42	4.32	2.23

General decay law: $\overline{u^2} = AU^2(x/M)^{-n}$

	A		n			A		n	
	(*a*)	(*b*)	(*a*)	(*b*)		(*a*)	(*b*)	(*a*)	(*b*)
$\overline{u_1^2}$	0.151	0.0300	1.33	1.25	$\overline{u_2^2}$	0.167	0.0843	1.29	1.46
$\overline{v_1^2}$	0.130	0.0238	1.30	1.25	$\overline{v_2^2}$	0.303	0.0656	1.51	1.41
$\overline{w_1^2}$	0.251	0.0235	1.49	1.26	$\overline{w_2^2}$	0.282	0.0577	1.53	1.39
k_1	0.268	0.0383	1.39	1.25	k_2	0.343	0.106	1.42	1.43

(*a*) 3.3:1 parallel bar grid, (*b*) 3:1 perforated plate

TABLE 1. Flow parameters for the three grids; k, ϵ and l are the turbulent kinetic energy, dissipation rate and integral lengthscale respectively; R_l and R_λ are the integral scale and Taylor Reynolds numbers, based on l and the Taylor microscale λ respectively; and τ is the integral timescale. Subscript 1 refers to the small-scale homogeneous region while subscript 2 refers to the large-scale homogeneous region. The general decay laws for the velocity variances and kinetic energy are also given for both the large- and small-scale homogeneous regions, for the 3.3:1 parallel bar grid and the perforated plate. The fluctuation parameters were evaluated at: (*a*) $x = 33.65M_2$ (106 cm), for the 3.3:1 bar grid; (*b*) $x = 21.4M_2$ (91 cm) for the 8.9:1 bar grid; and (*c*) $x = 19.4M_2$ (65 cm) for the perforated plate ($\nu = 1.6 \times 10^{-5}$ m^2/s and $\rho = 1.15$ kg/m^3).

grid solidity σ (here solidity is defined as the ratio of the closed area of the grid to the total area) for the three grids are documented in table 1. The construction of the grids is described in detail below. The mean velocity was approximately 6 m/s for all three experiments (Table 1). Conventional ×-hot wires were used, in conjunction with Dantec 55M01 constant-temperature anemometer bridges, to measure the U, u,

v and w velocity fields. The wires were made of tungsten with a diameter of 3.05×10^{-3} mm and a length-to-diameter ratio of approximately 200. The overheat ratio was 1.8. The velocity signals were band-pass filtered through Khronhite 3342 filters prior to digitization. The signals were digitized using an A-D converter (Digital Equipment Corporation, ADV11-DA) with an output resolution of 12 bits and a maximum speed of approximately 45 kHz. Two different sampling rates were used. To capture the full range of scales, a Nyquist frequency of 5 kHz was chosen for calculating the spectra and dissipation. For generating moments, on the other hand, a much smaller sampling rate (< 400 Hz) was used so that each sample was separated from its neighbours by at least one integral timescale. This separation in time is necessary for quick convergence of high-order moments of the velocity field (Tennekes & Lumley 1972). A calibration procedure based on the studies conducted by Champagne, Sleicher & Wehrmann (1967), and Champagne & Sleicher (1967) on inclined hot wires, was used to convert the instantaneous voltages into velocities. The results were analysed on a Micro Vax II computer.

3.1. *The parallel bar grids*

Parallel bar grids were used to generate the mixing layer rather than conventional biplanar grids as matching the mesh sizes and tuning the grid to obtain a constant mean field would have been extremely difficult with a biplanar grid. Even with parallel bar grids, obtaining the desired flow was not easy; a 0.5 mm change in bar position could change the mean velocity by 1.5% locally. The final adjustments to the grid spacings involved changes as small as 0.15 mm. Many months were spent in fine-tuning these grids. As discussed in V&W, there is an additional problem with parallel bar grids caused by the presence of large structures in the flow which originate from the vortices shed from the bars. Close to the grid the vortices are oriented parallel to the grid bars but the large-scale structures, arising from a complex interaction of these vortices, eventually align themselves perpendicular to the grid bars as a study of the two-point correlation functions $R_{11}(0, r, 0)$ and $R_{11}(0, 0, r)$ showed (V&W). When the aspect ratio (ratio of the width of the tunnel to the mesh spacing) is small (approximately less than 15), these structures (approximately 4 mesh sizes in width) convect turbulent energy from the centre of the flow to the wall regions. While the mean velocity field is essentially unaffected by this mixing, large unwanted gradients of the variance field are generated in the z-direction by it. The aspect ratio for the large-mesh region of the 3.3:1 grid was 13, while it was 9.5 for the 8.9:1 grid. Hence in both these grids the large-mesh region was susceptible to the problem discussed above. In an effort to break up these large structures and generate a more homogeneous flow, small blocks were glued onto the sides of the grid bars. The thicknesses of the blocks were 1.02 mm for the 3.3:1 grid (bar width = 9.53 mm) and 1.59 mm for the 8.9:1 grid (bar width = 11.11 mm). The blocks were placed approximately one mesh length apart in an effort to best simulate a crossed-bar grid and their thicknesses were determined by trial and error, so as to generate homogeneous mean and fluctuating velocity fields. Figure 2 shows in detail, the construction of the parallel bar grids. In V&W, a helically wound wire, with a lead of approximately 1 mesh length and a thickness approximately equal to that of the blocks mentioned above, was used to homogenize the flow. However, since the low-intensity region of the flow is most influenced by the winding closest to it, there is a tendency for this region of the flow to get skewed in the direction of the helix; hence, blocks were preferred in the present experiments. To reduce the effect of the blocks on the low-intensity region, the row of blocks closest to the small-mesh side

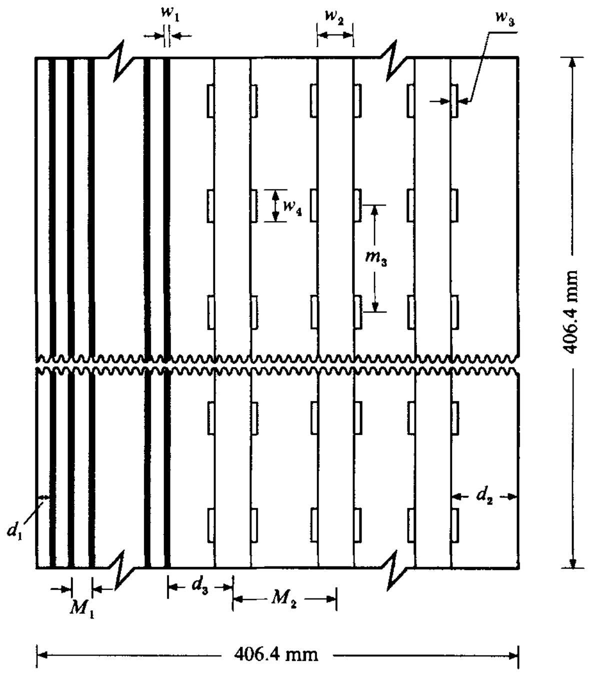

FIGURE 2. Sketch of the parallel bar grids showing the details of construction.

Grid	M_1	M_2	m_3	w_1	w_2	w_3	w_4	d_1	d_2	d_3	n_1	n_2
3.3:1	9.53	31.5	29.7	3.18	9.53	1.02	9.78	5.11	14.61	20.3	19	7
8.9:1	4.77	42.5	34.9	1.59	11.11	1.59	9.53	6.80	20.30	26.9	29	6

The number of small bars is n_1 and the number of large bars is n_2. The bars are square-sectioned and the blocks extend over the full width of the bars. All the dimensions above are in mm.

was omitted for the 3.3:1 grid. For the low-intensity side no blocks were needed since here the aspect ratio was high (39 for the 3.3:1 grid and 66.5 for the 8.9:1 grid).

3.2. *The perforated plate*

To study the influence of initial conditions and grid geometry on the development of the mixing layer, a perforated plate with a mesh ratio of 3:1 was also used to generate the flow. Figure 3 shows the details of construction of this grid. As shown in the figure the grid essentially consists of a plate with holes of two different sizes (the radii are 14.29 mm and 4.76 mm). The separation between the holes was chosen so as to obtain the same solidity (0.31) on both sides of the grid. At the centre of the grid small holes (radius 2.95 mm) were added to reduce the local solidity to 0.31. However, in spite of the care taken in manufacturing the grid, the resulting mean velocity field had local variations. These were largely eliminated by introducing 0.23 mm thick Mylar tubes into the large diameter holes (figure 3). When the tubes extended upstream of the plate, they caused the flow to slow down locally owing to an increased blockage, while, when the tubes extended downstream, they streamlined the flow causing it to increase locally. By trial and error the tube lengths and positions required for a homogeneous mean velocity field, were determined. These are shown in figure 3. Since the perforated plate behaves like a crossed-bar grid the problem of large-scale structures encountered with the parallel bar grids is absent here.

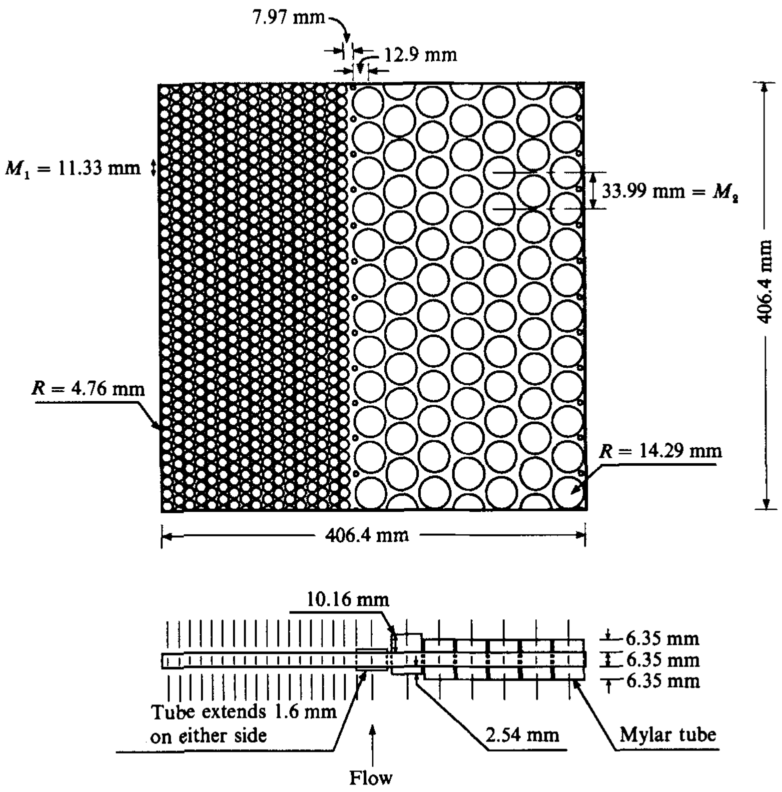

FIGURE 3. Sketch of the 3:1 perforated plate showing the details of construction. Also shown are the tubes in the large-diameter holes used to reduce mean velocity gradients. The tiny holes at the centre of the grid and at the large-scale edge of the grid are 2.95 mm in radius.

3.3. *Realization of the flow*

As discussed in §2 above, for an ideal turbulence mixing layer, the mean velocity gradients should be zero so that there is no production term in the kinetic energy budget, the flow should also be homogeneous in the z-direction so that gradients of all mean quantities are zero in that direction and the turbulent timescales should be the same at the two homogeneous edges of the flow.

Figure 4 shows a two-dimensional map of the mean velocity at $x = 65$ cm for each of the three grids. We note that all the three mean velocity fields are approximately homogeneous; the overall change in U is approximately 6% for the two parallel bar grids and 8% for the perforated plate. The maximum shear rate is nearly the same in each case (approximately 7/s). We will now consider the magnitude of the turbulence energy production term caused by these inhomogeneities in the mean flow. Figure 5(a) shows the profile of the $\overline{uv}$ correlation at $x = 49.5M_2$(156 cm) for the 3.3:1 grid (the production term is most significant at this location, for this grid). We see that the correlation, though small, is not insignificant; it attains a peak value of about 0.3 within the mixing layer. This might seem surprisingly high in the absence of large mean shear; however, as discussed in §2, a different mechanism for the generation of $\overline{uv}$ exists in this flow from the one present in normal shear flows. Figure 5(b) shows he ratio of the resulting production term $(-\overline{uv}\,\partial U/\partial y)$ to the dissipation (ϵ) at the same location. We see that this ratio is less than 7% throughout the flow.

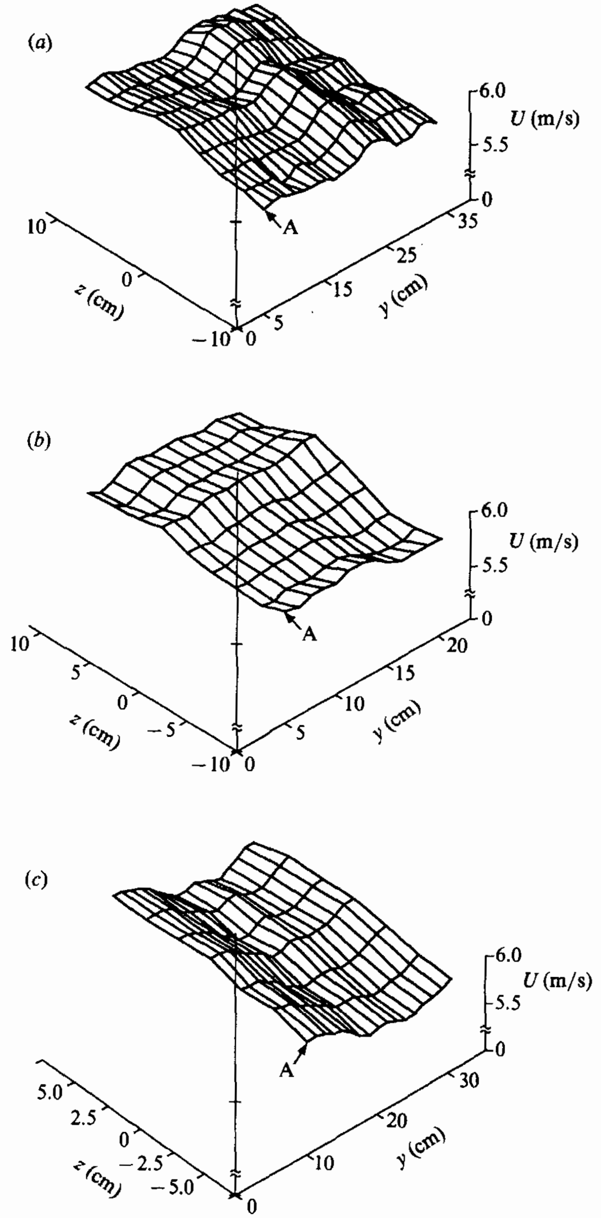

FIGURE 4. Two-dimensional maps of the mean velocity field for the three different grids at $x = 65$ cm. The measuring stations were spaced 1.27 cm apart in the y-direction and 2.54 cm apart in the z-direction. The coordinates of the nearest corner (marked A) are given below for each case. (*a*) 3.3:1 parallel bar grid, A $\equiv$ ($y = 5.08$ cm, $z = -10.16$ cm, $U = 5.95$ m/s); (*b*) 8.9:1 parallel bar grid, A $\equiv$ (5.08 cm, −10.16 cm, 6.04 m/s); (*c*) 3:1 perforated plate, A $\equiv$ (10.16 cm, −7.62 cm, 6.18 m/s).

Closer to the grid it was even smaller and hence the exclusion of the production term from the energy budget is justified throughout the region of study. The results (not shown) for the 8.9:1 parallel bar grid and the perforated plate indicate that production term is negligible for them also. However, for the perforated plate the relative (to ϵ) magnitude of the production term did increase with downstream

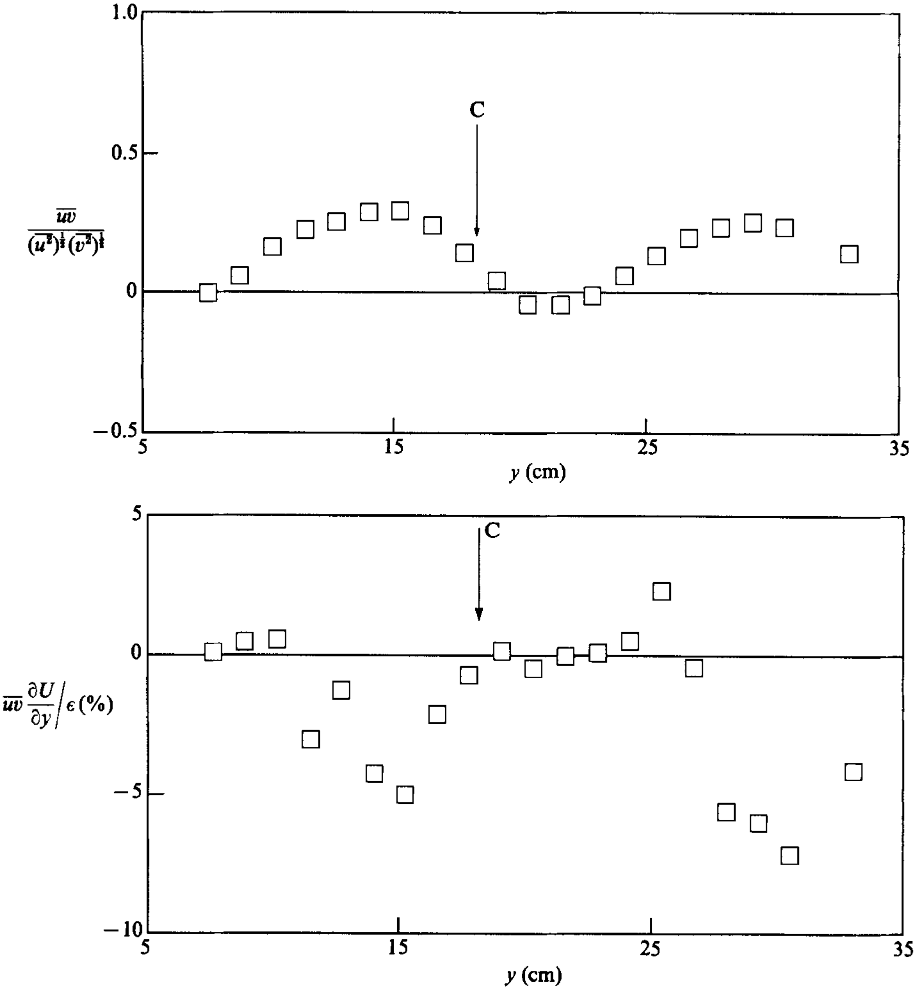

FIGURE 5. Profiles of (*a*) the $\overline{uv}$ correlation and (*b*) the ratio of production to dissipation for the 3.3:1 parallel bar grid at $x = 49.5M_2$ (156 cm). The arrow marked C denotes the geometric centre of the grid in each case i.e. the location where the mesh size changes.

distance and thus for this grid we were unable to measure beyond $x/M_2 = 36.7$. As will be shown in §4.2 this precluded the measurements reaching the self-similar range for this grid.

Figure 6 shows the two-dimensional map of the $(\overline{u^2})^{\frac{1}{2}}$ field for the three grids at $x = 65$ cm. At the two homogeneous ends of the mixing layer the variation with z is very small; it is always less than 5% and in some instances as low as 2%. Within the mixing layer however, larger variations with z are seen. The largest variation is approximately 15% for the two parallel bar grids and approximately 10% for the perforated plate. However, even for these cases the gradient in the y-direction is much larger than that in the z-direction (their ratio is always greater than 5). Hence, the gradients in the z-direction play a negligible role in the overall energetics of the flow. Furthermore, the homogeneity in the z-direction improves with increasing distance from the grid; figure 6 shows the worst case.

Finally, we note, from the values of $\tau_1(\equiv k_1/\epsilon_1)$ and $\tau_2(\equiv k_2/\epsilon_2)$ shown in table 1, that the requirement of equal timescales at the two homogeneous edges of the flow

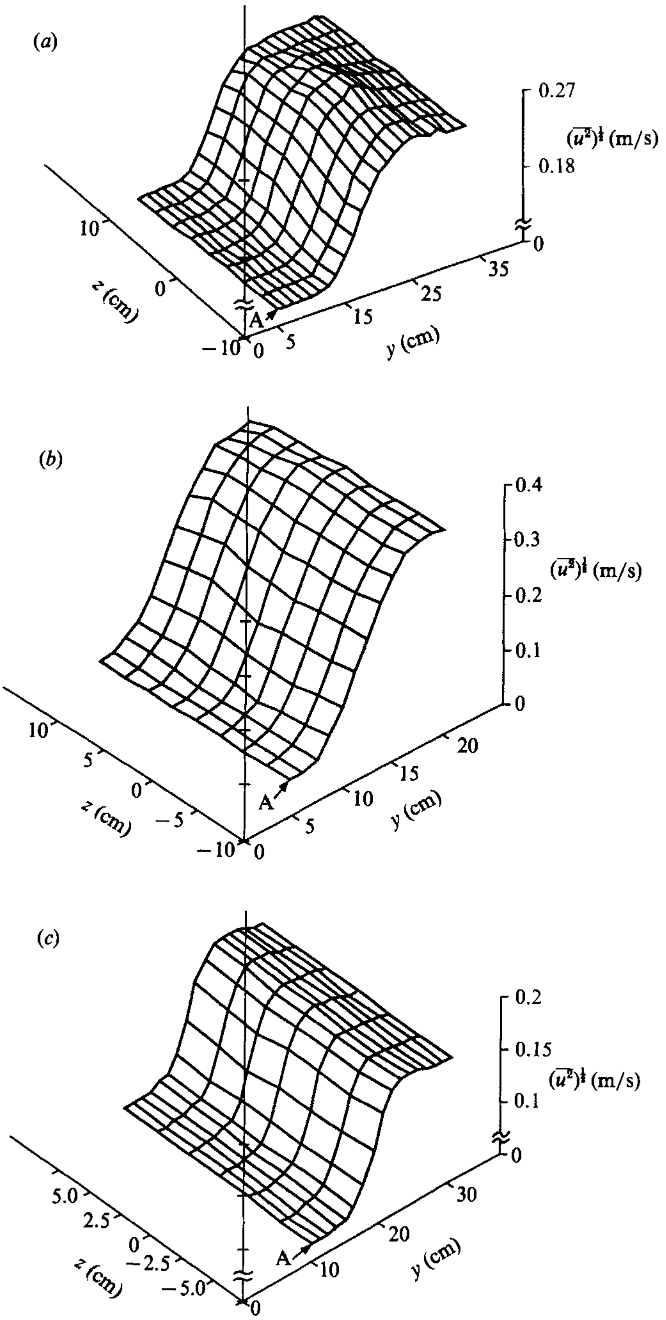

FIGURE 6. Two-dimensional maps of the longitudinal r.m.s. velocity field for the three different grids at $x = 65$ cm. The measuring stations were spaced 1.27 cm apart in the y-direction and 2.54 cm apart in the z-direction. The coordinates of the nearest corner (marked A) are given below for each case. (*a*) 3.3:1 parallel bar grid, $A \equiv (y = 5.08\text{ cm},\ z = -10.16\text{ cm},\ (\overline{u^2})^{\frac{1}{2}} = 0.116\text{ m/s})$; (*b*) 8.9:1 parallel bar grid, $A \equiv (5.08\text{ cm},\ -10.16\text{ cm},\ 0.060\text{ m/s})$; (*c*) 3:1 perforated plate $A \equiv (10.16\text{ cm},\ -7.62\text{ cm},\ 0.066\text{ m/s})$.

is approximately met. Table 1 also documents the flow Reynolds numbers, turbulence decay laws and other turbulence parameters for the homogeneous regions bounding the mixing layer for each of the three grids. The decay laws for the 8.9:1 bar grid are not given in table 1, since they could not be accurately determined owing to interference from the wall boundary layer.

4. The results

4.1. *The time series*

Before analysing the statistical properties of the data we shall first discuss some representative time series. Figure 7 shows the time series of u- and v-fluctuations for the 8.9:1 parallel bar grid at $x = 21.4M_2$ (91 cm). The figure juxtaposes flow histories obtained at three different lateral positions. The first station lies in the homogeneous low-turbulence region of the flow, the second location is within the mixing layer (it is at the position where $\overline{u^4}/(\overline{u^2})^2$ attains its maximum, see figure 12 below), and the third lies in the homogeneous high-turbulence region. The normalized time series, $u^3/(\overline{u^2})^{\frac{3}{2}}$, $u^4/(\overline{u^2})^2$, $v^3/(\overline{v^2})^{\frac{3}{2}}$ and $v^4/(\overline{v^2})^2$ are also shown in the figure. To permit comparison, the normalized time series within the mixing layer have been scaled down by a factor of 4 for the u-component and a factor of 15 for the v-component.

The time series in both the homogeneous low- and high-turbulence sides of the mixing layer are of the same form, and similar to what is normally observed in grid turbulence. The time series obtained in the mixing layer, however, are markedly different. These show intermittent bursts from the large-scale side with intervals of purely low-intensity fluctuations separating them. The high-intensity bursts are much larger in magnitude in the v-time series compared to those of the u-series. The bursts are predominantly negative in the v-series, while both positive and negative large-scale fluctuations from the high-turbulence side are present in the u-series. This is particularly evident in the $u^3/(\overline{u^2})^{\frac{3}{2}}$ and $v^3/(\overline{v^2})^{\frac{3}{2}}$ time series. The $u^4/(\overline{u^2})^2$ and $v^4(\overline{v^2})^2$ series also show strong intermittency in the mixing layer. These series are intermittent in the homogeneous regions too; however, there the large peaks are not as isolated and a hierarchy of peaks from very small to very large is seen.

The time series are further discussed in §4.3 below.

4.2. *The kinetic energy components*

We shall first compare the three kinetic energy components at one downstream location and then examine the evolution of these components with downstream position. Figure 8 shows typical cross-stream profiles of the variances of u-, v- and w-fluctuations at a fixed downstream location for each of the three grids. The measurements were done at $x = 33.7M_2$ (106 cm) for the 3.3:1 grid, $x = 28.9M_2$ (123 cm) for the 8.9:1 grid and $x = 27.2M_2$ (91 cm) for the 3:1 perforated plate.

In all the three cases, $\overline{u^2}$ is larger than $\overline{v^2}$ and $\overline{w^2}$ at the two homogeneous ends of the mixing layer. This is consistent with measurements of biplanar grids by other researchers (Comte-Bellot & Corrsin 1966). Within the mixing layer, however, $\overline{v^2}$ is larger than $\overline{u^2}$ for the parallel bar grids. The v-component of the fluctuating velocity is chiefly responsible for transport across the mixing layer and since it is perfectly correlated with itself, it transports itself more effectively than it does u- and w-fluctuations. Hence v-fluctuations penetrate more deeply into the small-scale side of the mixing layer and consequently the $\overline{u^2}$ and $\overline{v^2}$ profiles cross over in the mixing layer. This effect is not as clearly seen in the case of the perforated plate. At larger x, however, $\overline{v^2}$ becomes perceptibly larger than $\overline{u^2}$ in the mixing layer for this case too.

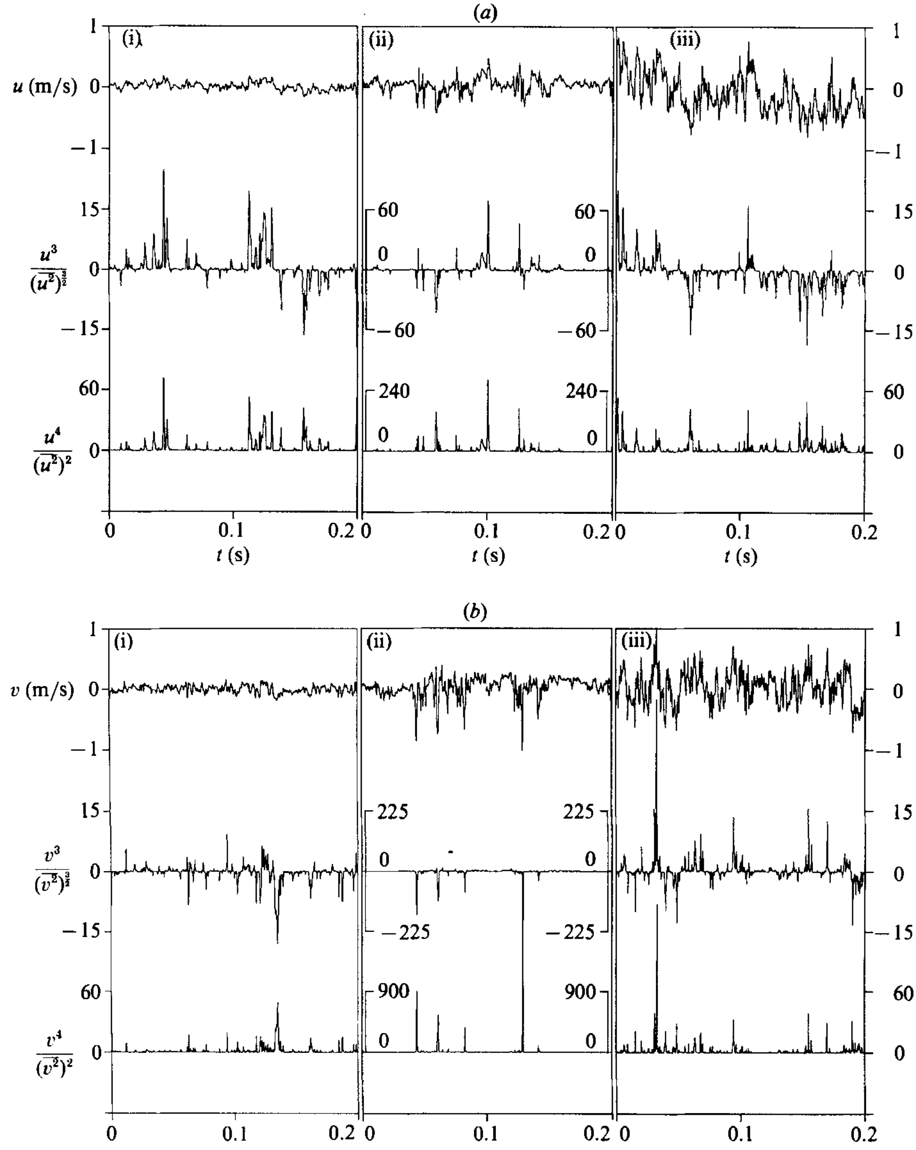

FIGURE 7. Typical time series of (a) u, $u^3/(\overline{u^2})^{\frac{3}{2}}$ and $u^4/(\overline{u^2})^2$ and (b) v, $v^3/(\overline{v^2})^{\frac{3}{2}}$ and $v^4/(\overline{v^2})^2$ for the 8.9:1 parallel bar grid at $x = 21.4M_2$ (91 cm) at three lateral positions: (i) $y = 5.08$ cm; (ii) $y = 8.89$ cm; (iii) $y = 22.9$ cm.

The difference in behaviour is probably due to the fact that the flow for this grid is in an earlier stage of development compared to those of the parallel bar grids (see following discussion). Notice the presence of bumps towards the large-scale ends of the mixing layers, particularly for the 3.3:1 bar grid and the perforated plate. These will be discussed below.

The arrows in figure 8 marked I locate the inflection points of the variance profiles and the arrow marked C shows the geometric centre of the grid, i.e. where the grid changes mesh size. We note that almost all the inflection points are located well towards the small-scale side of the geometric centre. This behaviour is particularly pronounced for the $\overline{v^2}$ profiles of the parallel bar grids. The asymmetry noted here is consistent with our preliminary observations made earlier (V&W).

Figure 9 shows normalized $\overline{u^2}$, $\overline{v^2}$ and $\overline{w^2}$ variance profiles taken at three downstream locations for the three different grids. The collapse is achieved by first normalizing the variance by the asymptotic values attained by the profiles at the large-scale homogeneous end of the flow ($\overline{u_2^2}$, $\overline{v_2^2}$ and $\overline{w_2^2}$). The curves are then centred about their respective inflection points. Finally, the lateral spread is non-dimensionalized by the lengthscale $l_{\frac{1}{2}}$, which is obtained by mapping the small-scale end of the variance profile to zero and the large-scale end to one. The horizontal distance between the points with ordinate values of 0.25 and 0.75 is then the required $l_{\frac{1}{2}}$. This lengthscale was obtained from the $\overline{u^2}$ profile alone but used to collapse the profiles of all three energy components. The lengthscale may be viewed as a simple generalization of the half-length used to characterize symmetric profiles, found in jets and wakes, etc. Table 2 contains all the information relevant to the procedure discussed above, i.e. the normalizing length and velocity scales and the locations of the inflexion points.

The collapse is remarkably good for all the three components and for all the three grids. It should be noted that since $l_{\frac{1}{2}}$ was obtained from the $\overline{u^2}$ profile alone but used to normalize the profiles of all three energy components the collapse of the data indicates that the individual lengthscales grow at the same rate. We shall see in §4.5, however, that the local lengthscales of u, v and w vary in very different ways across the layer.

The solid lines shown in figure 9 represent the best error-function fits (obtained by minimizing the mean-square error) to the collapsed profiles. The upper and lower limits of the error functions were fixed at the values attained by the respective variances in the high- and low-intensity homogeneous regions of the flow. It is clear that an error function does not provide a good fit to the profiles of the 3.3:1 parallel bar grid or the perforated plate. In both these cases the most significant departure from an error function is on the high-turbulence side of the flow where an overshoot or a 'bump' occurs in the profiles. This was also observed in our earlier measurements (V&W) with a parallel bar grid. For both the 3.3:1 bar grid and the 3:1 perforated plate, the lengthscale ratio (l_2/l_1) is sufficiently large, 2.4 and 2.2 respectively (table 1), that we could expect asymmetry in the variance profiles because of the presence of two distinct scales. A simple mixing-length type analysis, wherein the lengthscale is allowed to vary smoothly from a small value in the low-turbulence homogeneous region to a large value in the high-turbulence homogeneous region, would yield a variance profile similar to the $\overline{u^2}$ profile of the 3.3:1 parallel bar grid. Here, the profile is steeper than the best fit error function on the low-turbulence side of the mixing layer while it is shallower than the error function on the high-turbulence side. It is not clear why the strong interaction of the two scales also produced the 'bump' in the variance profiles.

For the 8.9:1 bar grid (figure 9*b*), however, an error-function fit is good. Here the lengthscale ratio is approximately 4.3 (table 1) and the turbulence energy ratio is approximately 22 (see table 3, §4.3 below). (The corresponding ratios for the 3.3:1 parallel bar grid are 2.4 and 6.2 respectively.) Clearly, then, the large scale dominates the energetics of the flow for the 8.9:1 grid and the mixing layer is essentially controlled by a single scale. We shall give further evidence of this when we examine the lateral variation of the lengthscales in §4.5.

The profiles of Gilbert (1980) were also well represented by an error function, suggesting that there too the mixing process was controlled by a single scale.

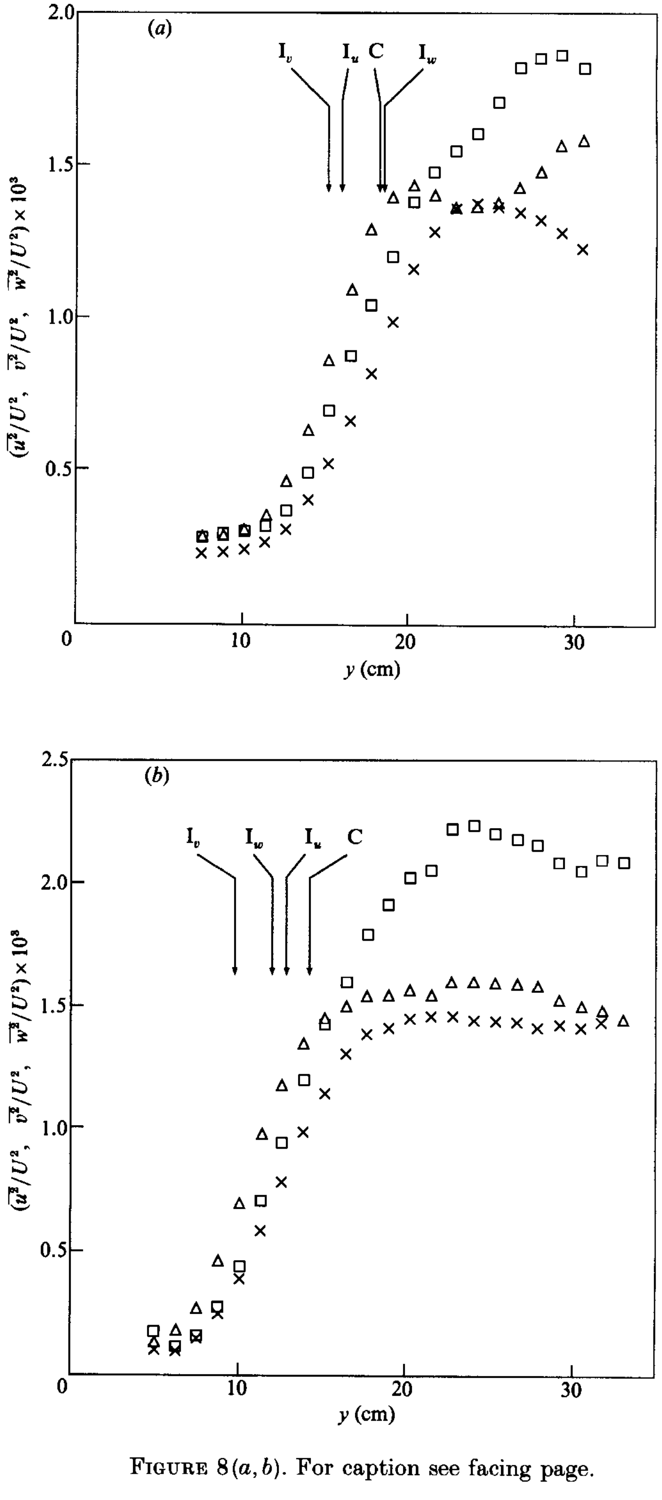

FIGURE 8(*a*, *b*). For caption see facing page.

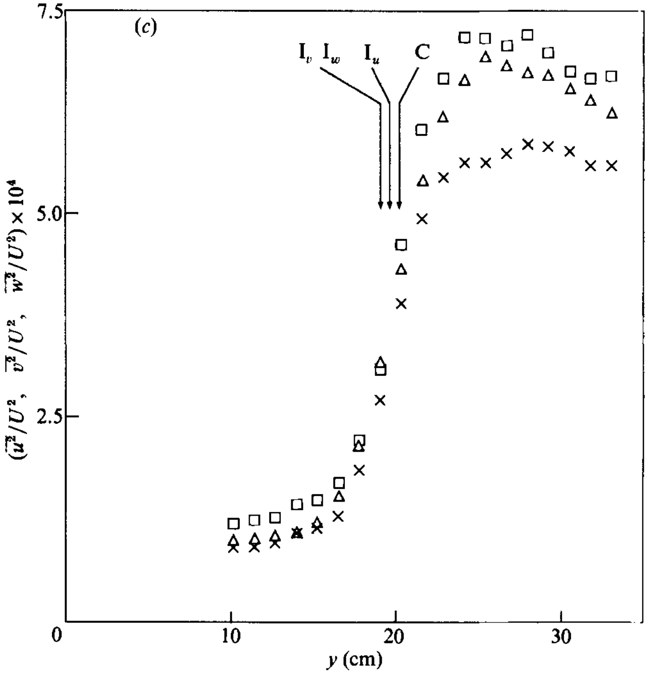

FIGURE 8. Profiles of the variances $\overline{u^2}$, $\overline{v^2}$ and $\overline{w^2}$, normalized by U^2 for the three different grids. (*a*) 3.3:1 parallel bar grid; $x = 33.65M_2$ (106 cm), (*b*) 8.9:1 parallel bar grid; $x = 28.9M_2$ (123 cm) and, (*c*) 3:1 perforated plate; $x = 27.2M_2$ (91 cm). The arrows marked I_u, I_v and I_w indicate the locations of the inflection points of the $\overline{u^2}$, $\overline{v^2}$ and $\overline{w^2}$ profiles, respectively. The arrow marked C shows the location of the geometric centre of the grid. The symbols are: □, $\overline{u^2}/U^2$; △, $\overline{v^2}/U^2$; and ×, $\overline{w^2}/U^2$.

However, in contrast to our 8.9:1 grid, for Gilbert's experiment the mesh ratio was only 2, giving a lengthscale ratio of 1.4, a value too close to unity to discern pronounced two-scale interaction.

It appears, then, that there is a distinct range of lengthscale ratios over which two scales are dominant and the resulting profiles are asymmetric. As this ratio approaches unity (as in Gilbert 1980), the flow is essentially that of a single scale (although the magnitudes of the variances on either side of the mixing layer are different), while as the lengthscale ratio becomes very large, the flow is again dominated by a single lengthscale. This is the case for the 8.9:1 parallel bar grid.

Figure 10(*a*) shows the variation of $l_{\frac{1}{2}}$ with the convection time x/U for the three grids. The half-width has been normalized by l_2, the integral lengthscale on the large-scale side. As shown in table 1, l_2 has been defined as $k_2^{\frac{3}{2}}/\epsilon_2$ and was obtained from the respective decay laws.† The mixing layer of the 3.3:1 bar grid appears to have reached a self-similar state and the flow for the 8.9:1 bar grid also seems to be approaching self-similarity. However, the flow is clearly not self-similar for the 3:1 perforated plate because the two lengthscales ($l_{\frac{1}{2}}$ and l_2) are growing at different rates. Notice that the ratio $l_{\frac{1}{2}}/l_2$ asymptotes to a larger value for the 3.3:1 bar grid than for the 8.9:1 bar grid. The reason for this is that both scales are involved in spreading

† As mentioned in §3, the decay laws for the 8.9:1 bar grid could not be accurately determined because of boundary-layer interference. Hence, for this grid l_2 was obtained using an estimate of ϵ_2 from velocity derivatives and assuming a lengthscale growth rate of $x^{0.3}$ (i.e. the same as the other grids). Both methods of estimating l_2 agree to within a few percent for the 3.3:1 bar grid.

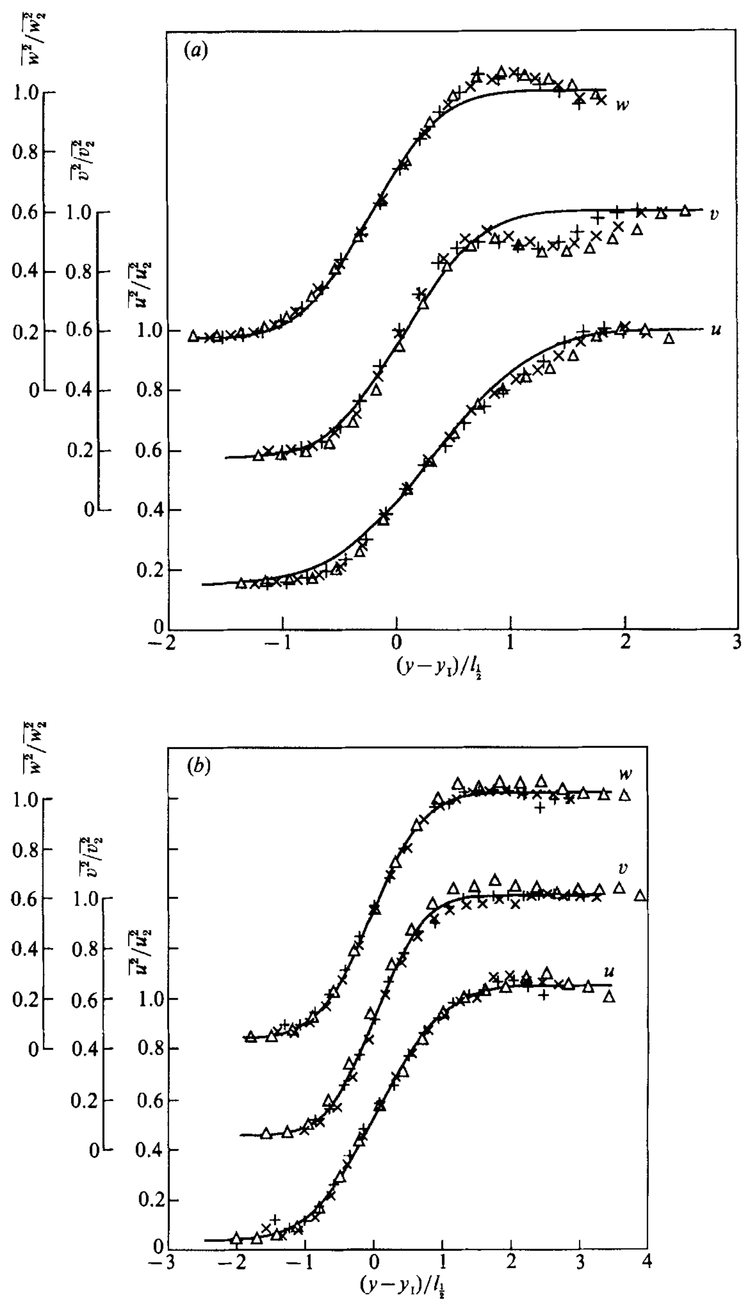

FIGURE 9(*a*, *b*). For caption see facing page.

the mixing layer in the case of the 3.3:1 bar grid, while, for the 8.9:1 bar grid, the large scale accounts almost entirely for the spreading. (Note that the use of l_1 as the normalizing lengthscale would have been just as appropriate and in this case the asymptote would have been larger for the 8.9:1 bar grid.) Since the length- and velocity-scale ratios are very similar for the 3.3:1 bar grid and the 3:1 perforated plate, we could expect the same asymptotic behaviour for both these flows. However,

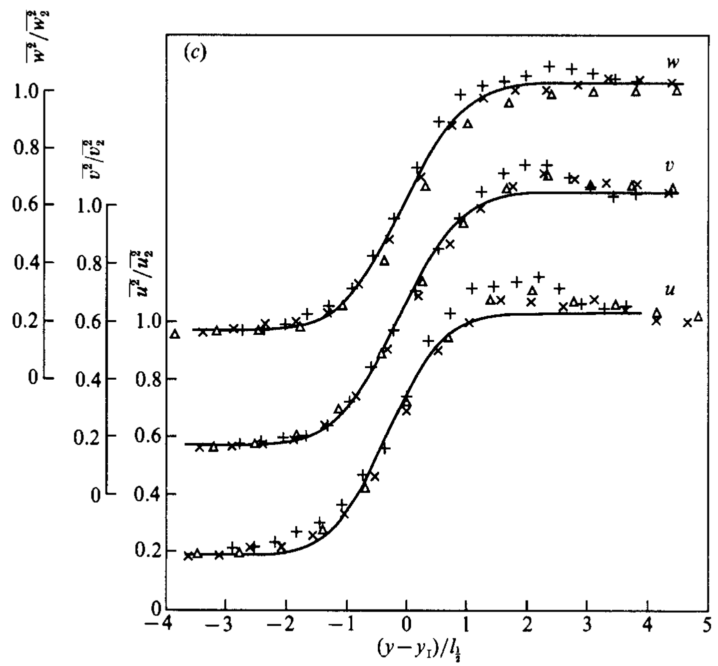

FIGURE 9. Normalized variance profiles for the three different grids. The variances $\overline{u^2}$, $\overline{v^2}$ and $\overline{w^2}$ have been normalized by the values attained in the large-scale homogeneous region, i.e. by $\overline{u_2^2}$, $\overline{v_2^2}$ and $\overline{v_2^2}$, respectively. The lateral coordinate has been centred about the inflection point of the respective variance profile and normalized by the half-width $l_{\frac{1}{2}}$ (see §4.2). The solid lines represent best error-function fits to the data. (*a*) 3.3:1 bar grid; △, $x = 33.65M_2$ (106 cm); ×, $x = 41.59M_2$ (131 cm); +, $x = 49.5M_2$ (156 cm). (*b*) 8.9:1 bar grid; △, $x = 21.4M_2$ (91 cm); ×, $x = 28.9M_2$ (123 cm); +, $x = 36.7M_2$ (156 cm). (*c*) 3:1 perforated plate; △, $x = 19.4M_2$ (65 cm); ×, $x = 27.2M_2$ (91 cm); +, $x = 36.7M_2$ (123 cm).

						Inflection point locations			
x (m)	x/M_1	x/M_2	$\overline{u_2^2}$ (m²/s²)	$\overline{v_2^2}$ (m²/s²)	$\overline{w_2^2}$ (m²/s²)	I_u (cm)	I_v (cm)	I_w (cm)	$l_{\frac{1}{2}}$ (cm)
				(*a*) 3.3:1 parallel bar grid					
1.06	111.6	33.65	0.065	0.055	0.046	15.9	15.0	18.5	6.10
1.31	137.9	41.59	0.046	0.037	0.033	15.9	15.0	18.5	6.62
1.56	164.2	49.52	0.038	0.031	0.026	15.9	15.0	18.7	7.30
				(*b*) 8.9:1 parallel bar grid					
0.91	190.78	21.4	0.108	0.082	0.077	12.9	11.1	12.0	4.18
1.23	257.86	28.9	0.071	0.055	0.050	12.9	9.9	12.0	5.35
1.56	327.04	36.7	0.053	0.038	0.035	12.9	9.5	12.0	5.80
				(*c*) 3:1 perforated plate					
0.65	58.04	19.4	0.037	0.033	0.032	19.7	19.2	19.1	1.83
0.91	81.25	27.2	0.023	0.022	0.020	19.7	19.2	19.1	2.45
1.23	109.8	46.6	0.013	0.012	0.012	19.7	19.2	19.1	3.5

TABLE 2. Normalization parameters for the three grids

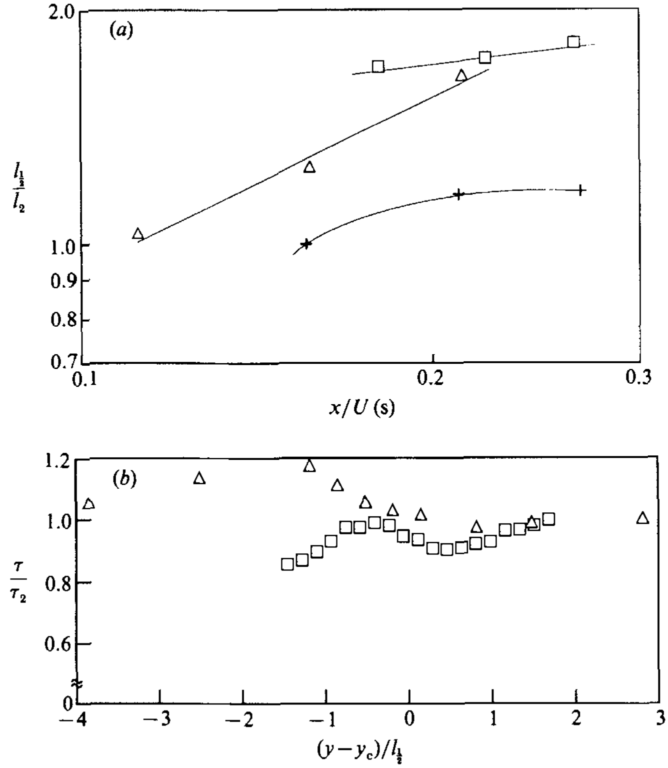

FIGURE 10. (*a*) The evolution of the half-width ($l_{\frac{1}{2}}$) normalized by the integral lengthscale l_2, for the three grids. □, 3.3:1 parallel bar grid; +, 8.9:1 parallel bar grid; △, 3:1 perforated plate. Note: the scales are logarithmic. (*b*) The variation of the integral timescale τ ($\equiv k/\epsilon$), normalized by its value in the large-scale homogeneous region, across the mixing layer. □, 3.3:1 parallel bar grid, $x = 49.5M_2$ (156 cm); △, 3:1 perforated plate, $x = 20.4M_2$ (68.5 cm).

because of the way in which the grids were constructed, it was possible to generate a much sharper transition from one scale to the other with the perforated plate. Thus the initial value of $l_{\frac{1}{2}}/l_2$ was further away from its asymptotic limit (assuming it exists) for the 3:1 perforated plate, which accounts for its rapid growth and lack of self-similarity in the region of study. It is possible that had we been able to measure further downstream for the perforated plate, we would have seen a tendency towards self-similarity for this flow too.

Figure 10(*b*) shows the variation of the ratio of the integral timescales, τ_1/τ_2 ($\equiv (k_1/\epsilon_1)/(k_2/\epsilon_2)$) for the 3.3:1 bar grid and the 3:1 perforated plate, across the mixing layer. The downstream locations are: $x = 49.5M_2$ (156 cm) for the 3.3:1 bar grid and $x = 20.4M_2$ (68.5 cm) for the 3:1 perforated plate. The timescales should be approximately equal at the two homogeneous edges of the mixing layer since the power-law decay exponents are nearly the same (see table 1). It is interesting to see that the ratio τ_1/τ_2 is close to unity in the mixing layer too. The overall variation is less than 20% in each of the cases shown. We note that figure 10(*a*) indicates that the mixing layer of the 3.3:1 bar grid is nearly self-similar at $x = 49.5M_2$ while it is clearly not self-similar at $x = 20.4M_2$ for the perforated plate. Thus it appears that the behaviour of the time scale ratio is insensitive to the state of development of the mixing layer, i.e. whether or not it is in the self-similar regime.

4.3. *The skewness and the kurtosis*

Figure 11 shows the variation of the skewness of u-, v- and w-fluctuations, S_u, S_v and S_w, respectively, across the mixing layer for the three different grids. The skewness is defined in the usual way as $S_u = \overline{u^3}/(\overline{u^2})^{\frac{3}{2}}$ (and similarly for S_v and S_w). Here the collapse has been achieved by first fixing the origin of the abscissa at the location of the inflection point of the corresponding variance profile, and then normalizing the widths of the graphs by $l_{\frac{1}{2}}$ obtained from the $\overline{u^2}$ profile at the same downstream location. The downstream locations and symbols are the same as in figure 9. The collapse is excellent in all the cases suggesting that the asymptotic values of the skewnesses have been attained. The data show some scatter on the low-turbulence side for the 8.9:1 bar grid due to interference from the wall boundary layer. For all the profiles the skewness values are zero at the two homogeneous ends as expected.

First we shall discuss the S_v profiles. The large negative values of S_v are due to the fact that in the low-turbulence side of the mixing layer, large deviations from zero in the v-time series (figure 7*b*) are more likely to have originated from the large-scale side and hence are more likely to be negative. (A similar argument was used by Corrsin 1950, to estimate the skewness of transverse velocity fluctuations in weakly inhomogeneous turbulent shear flows.) As the energy ratio increases, the magnitude of the maximum departure from zero also increases. Thus the value of the extremum of S_v for the 8.9:1 bar grid is -2.5, while it is -1.2 for the 3.3:1 bar grid and approximately -0.8 for the 3:1 perforated plate. The lateral gradient of $\overline{v^3}$ is one of the principal contributors to the transport of kinetic energy across the mixing layer. This is discussed in §4.4 below.

The effects giving rise to S_u are of a more subtle nature. Since the flow is only weakly inhomogeneous in the x-direction, we would expect a near zero value of S_u throughout the mixing layer. However, figure 11 shows a significant region of negative values of S_u for both the parallel bar grids and both regions of positive and negative values of S_u for the perforated plate. The magnitudes of the negative peaks are -0.65 for the 3.3:1 bar grid, -0.55, for the 8.9:1 bar grid, and -0.3 for the 3:1 perforated plate. While the magnitude of S_u is significantly smaller than that of S_v, it is still much larger than 0.04, the maximum value reported for decaying homogeneous grid turbulence (Maxey 1986).

The reason for the departure of S_u from zero appears to be due to the presence of the non-zero (but small) Reynolds stress $\overline{uv}$ (figure 5*a*). The mechanism by which the $\overline{uv}$ correlation is generated has been discussed in §§2 and 3 above. The transport equation for $\overline{u^3}$ (equation (5*a*)) then indicates that the production term $\overline{uv}\,\partial/\partial y\,(\overline{u^2})$ is also not zero in the mixing layer. Equation (3) is consistent with a positive value of $\overline{uv}$ across most of the mixing layer (confirmed by our observations; figure 5*a*), which in turn implies that the production term $\overline{uv}\,\partial/\partial y\,(\overline{u^2})$ is predominantly positive and this is in agreement with the negative sign of S_u in figure 11. The region of positive S_u seen in the case of the perforated plate (figure 11*c*), decays with increasing downstream distance x, while the negative peak is approximately constant with x. It is unclear why this positive region occurs close to the grid. We note that while $\overline{uv}$ plays a crucial role in the $\overline{u^3}$ budget, it is dynamically insignificant in the kinetic energy budget as a comparison of the production and dissipation terms showed (figure 5*b*). Furthermore, the downstream transport of kinetic energy due to the gradient of $\overline{u^3}$ is also insignificant compared to the lateral transport due to $\partial/\partial y(\overline{u^2v})$ (see §4.4 below).

Finally, S_w should be identically zero for the whole flow from symmetry

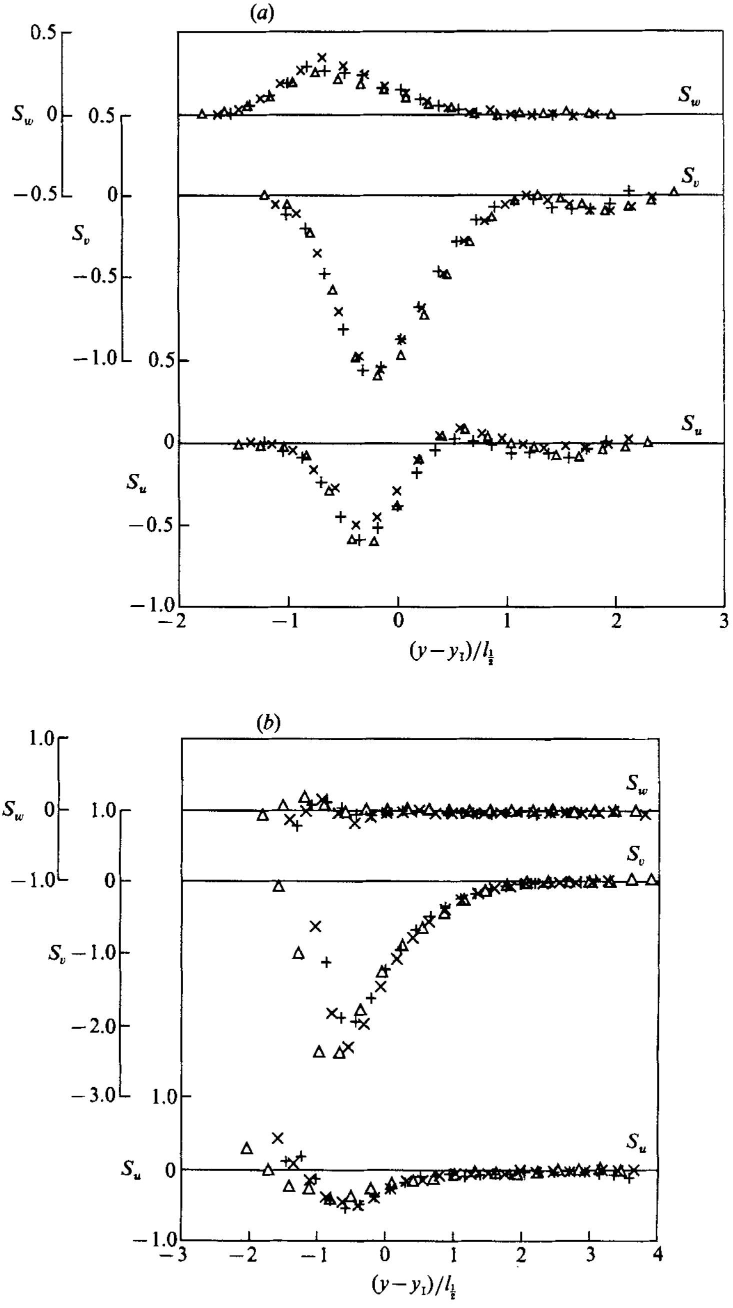

FIGURE 11 (*a*, *b*). For caption see facing page.

considerations. However, it attains a small peak value of 0.3 for all three grids. We do not understand the reason for this behaviour, but we note that it seems to be independent of the mode of turbulence generation since it is present for all three grids.

The profiles of the kurtosis (also called the flatness factor) of u-, v- and w-fluctuations, K_u, K_v and K_w respectively, for the three different grids are shown in

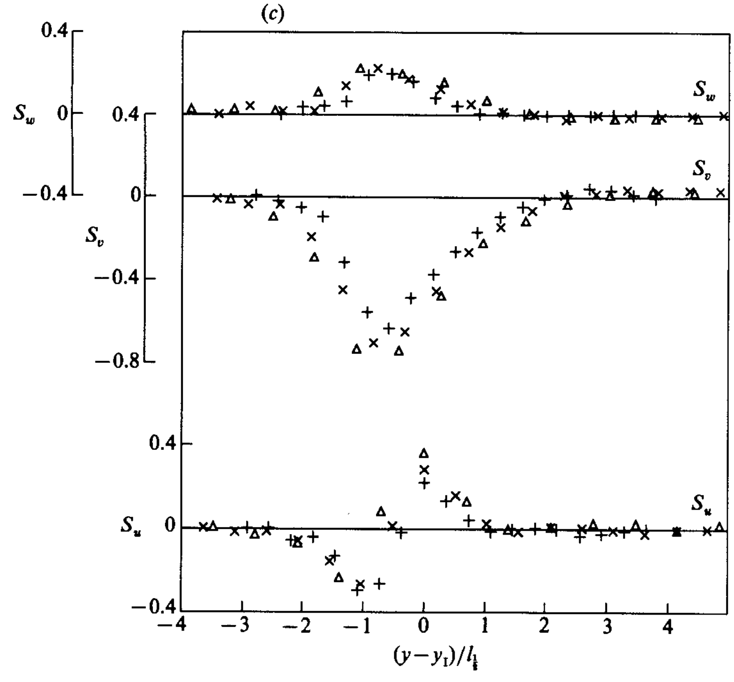

FIGURE 11. Profiles of S_u, S_v and S_w for the three different grids. The origin of the abscissa has been shifted to the location of the inflexion point of the corresponding variance profile (figure 9) and the abscissa has been normalized by $l_{\frac{1}{2}}$ in each case. (*a*) 3.3:1 bar grid, (*b*) 8.9:1 bar grid and (*c*) 3:1 perforated plate. In (*a*), (*b*) and (*c*), the symbols indicate the same downstream locations as those in figures 9(*a*), 9(*b*) and 9((*c*) respectively.

figure 12. The kurtosis is the normalized fourth moment; $K_u \equiv \overline{u^4}/(\overline{u^2})^2$ (and defined similarly for K_v and K_w). The method used in collapsing these profiles is the same as that employed for the skewness profiles (figure 11).

At the two homogeneous ends the turbulence is nearly Gaussian and K_u, K_v and K_w are approximately 3 in these regions for all three grids. Within the mixing layer, however, the curves show significant departures from 3. We note that the peaks of all the three curves lie well towards the small-scale side of the mixing layer. The collapse is excellent for the 3.3:1 bar grid (figure 12*a*). Like the skewness profiles (figure 11*b*), the kurtosis profiles for the 8.9:1 parallel bar grid (figure 12*b*) show small scatter on the low-turbulence side due to interference from the wall boundary layer. The kurtosis profiles for the perforated plate, especially those of K_v, show a systematic decay of the peak value with increasing x. This lends further credence to the observation made in §4.2 that this mixing layer is in an earlier stage of development than those of the parallel bar grids. (A small amount of decay can also be seen in the profiles of S_v (figure 11*c*) for the perforated plate, but the change is much more marked in the case of K_v (figure 12*c*).)

As shown in V&W, the form of the K_u and K_w profiles may be understood as follows: if it is assumed that the mixing process consists of only penetration (of the two scales into one another), rather than by penetration and turbulent diffusion, then the p.d.f. of the velocity fluctuations within the mixing layer is given by linear combination of the p.d.f.s at the two homogeneous edges. If we define r as the

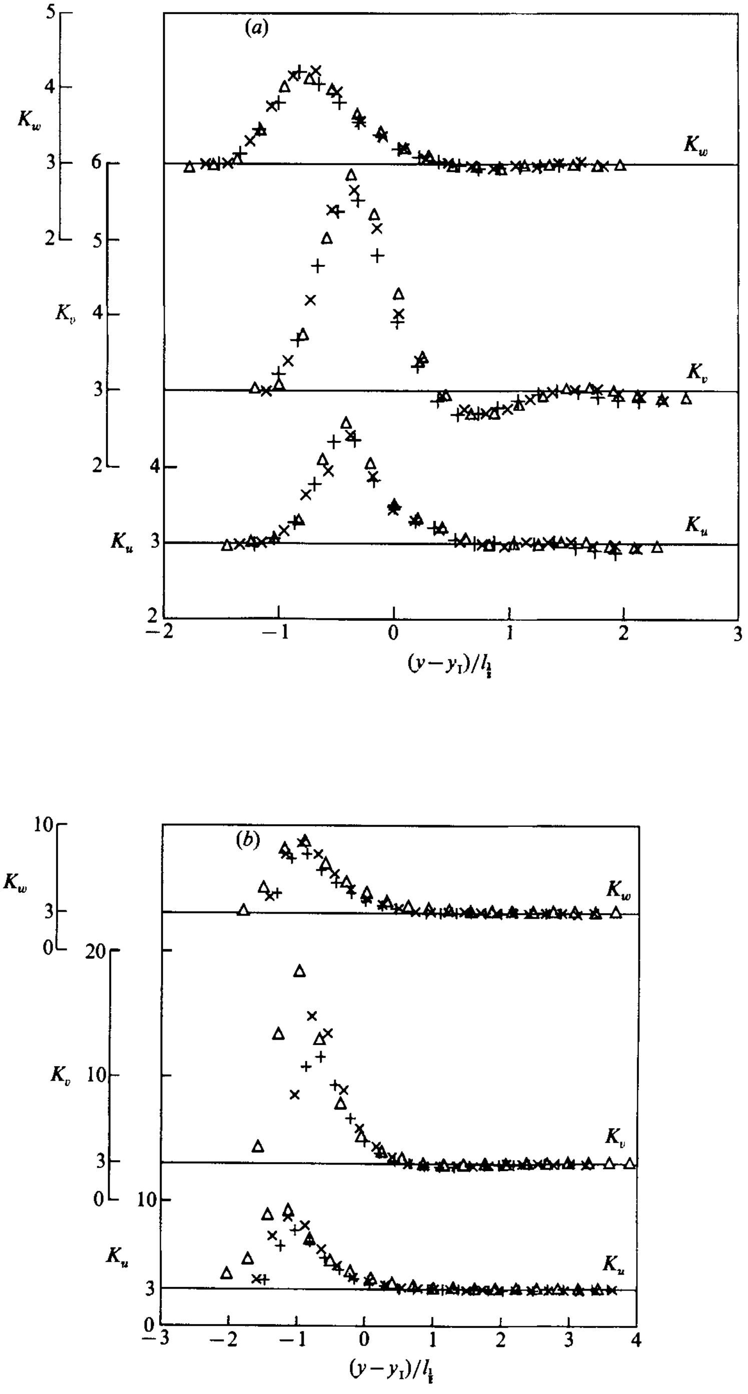

FIGURE 12(*a*, *b*). For caption see facing page.

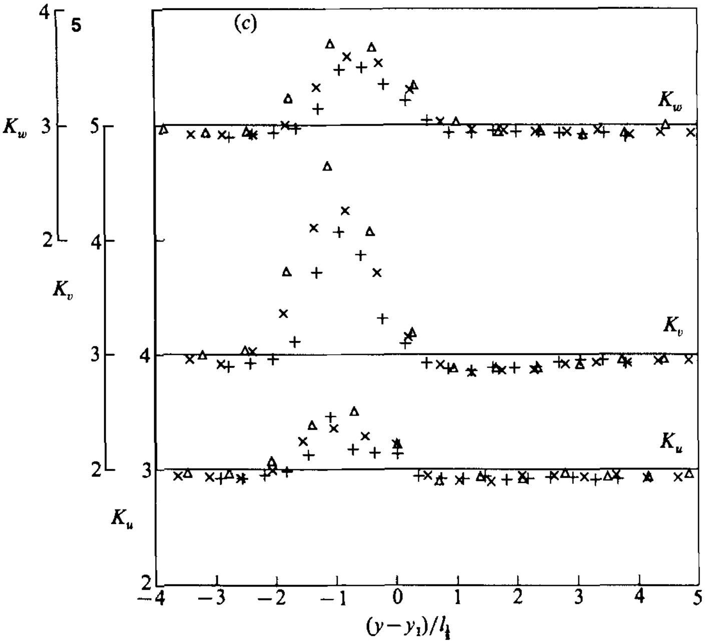

FIGURE 12. Profiles of the K_u, K_v and K_w for the three different grids. The origin of the abscissa has been shifted to the location of the inflexion point of the corresponding variance profile (figure 9) and the abscissa has been normalized by $l_{\frac{1}{2}}$ in each case. (*a*) 3.3:1 bar grid, (*b*) 8.9:1 bar grid and (*c*) 3:1 perforated plate. In (*a*), (*b*) and (*c*), the symbols indicate the same downstream locations as those in figures 9(*a*), 9(*b*) and 9(*c*) respectively.

intermittency factor of the large scale then the kurtosis within the mixing layer is given by

$$K_u(r) \equiv \frac{\overline{u^4(r)}}{(\overline{u^2(r)})^2} = \frac{\overline{u_2^4}\,r+\overline{u_1^4}\,(1-r)}{(\overline{u_2^2}\,r+\overline{u_1^2}\,(1-r))^2}$$

$$= \frac{3(\overline{u_2^2})^2\,r+3(\overline{u_1^2})^2\,(1-r)}{(\overline{u_2^2}\,r+\overline{u_1^2}\,(1-r))^2}$$

$$= \frac{3(R^4r+1-r)}{(R^2r+1-r)^2}, \tag{7}$$

where

$$R \equiv (\overline{u_2^2})^{\frac{1}{2}}/(\overline{u_1^2})^{\frac{1}{2}}. \tag{8}$$

(We have used the observed fact that the p.d.f.s at the two homogeneous ends are Gaussian and that their r.m.s. values are $(\overline{u_1^2})^{\frac{1}{2}}$ and $(\overline{u_2^2})^{\frac{1}{2}}$.) K attains its maximum at $r_{\mathrm{m}} = 1/(R^2+1)$ and its value there is

$$K_{\mathrm{m}} = \frac{3}{4}\frac{(R^2+1)^2}{R^2}. \tag{9}$$

Figure 13 shows a comparison of the K_u and K_w profiles for the 3.3:1 grid at $x = 33.65M_2$, with our estimates, calculated from (7). The intermittency factor r has been calculated from the variance profiles at the same location using the relation

$$r = \frac{\overline{u^2(r)}-\overline{u_1^2}}{\overline{u_2^2}-\overline{u_1^2}}. \tag{10}$$

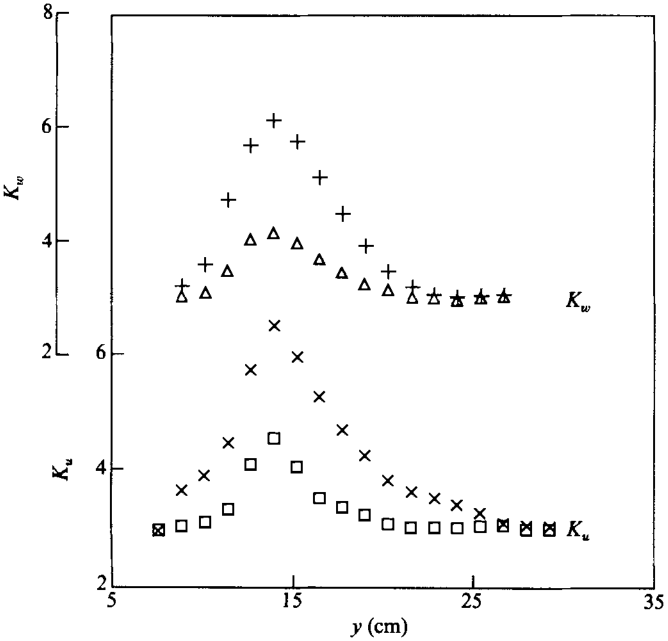

FIGURE 13. K_u and K_w compared with their estimates (equation (7)) for the 3.3:1 parallel bar grid at $x = 33.65M_2$ (106 cm). □, K_u; ×, K_u (estimated); △, K_w; +, K_w (estimated).

There is good qualitative agreement between the estimated and experimental curves. The locations of the peaks are predicted very well. However, the peak values are much lower in the experimentally obtained curves. This is because mixing takes place by both penetration and turbulent diffusion mechanisms. If only diffusion were important, the kurtosis profiles would not deviate from the Gaussian value of 3. If penetration were solely responsible for the mixing, the kurtosis profile would be given by (7). Since both mechanisms are present in the experiment, we observe an intermediate value for the kurtosis peak.

A convenient measure of the relative importance of penetration to the mixing process, is the kurtosis excess factor defined as K-3. In table 3 the peak excess factors of K_u and K_w are compared with their estimates obtained from (9). As expected, the peak values are much higher for the 8.9:1 bar grid due to its larger energy ratio. However, the ratio of the estimated peak to the experimental peak is approximately the same for the two parallel bar grids, indicating that the relative importance of penetration is roughly the same for both these grids. It is not clear why the peak values of the excess factors are much lower for the 3:1 perforated plate when compared with those of the 3.3:1 bar grid though the energy ratios are approximately the same (table 3). In Gilbert's experiment the variance ratio was very small; approximately 1.6. Equation (9) then indicates that the peak excess factor should not exceed 0.17, which is why he did not observe any systematic departures from a Gaussian distribution in the mixing layer.

Finally, we consider why in the mixing layer K_v is much larger than K_u and K_w (figure 12). To simplify the discussion we shall assume that only negative v-fluctuations from the high-turbulence side penetrate the low-turbulence side of the mixing layer (this assumption is sound as the time series in figure 7 show). Then, at any point on the small-scale side of the mixing layer, a cut-off velocity V_f may be

Grid	x/M_2	$\dfrac{\overline{u_2^2}}{\overline{u_1^2}}$	$\dfrac{\overline{v_2^2}}{\overline{v_1^2}}$	$\dfrac{\overline{w_2^2}}{\overline{w_1^2}}$	$\dfrac{k_2}{k_1}$	$K^{\mathrm{E}}_{u\mathrm{m}}$-3	$K^{\mathrm{E}}_{w\mathrm{m}}$-3	$K^{\mathrm{T}}_{u\mathrm{m}}$-3	$K^{\mathrm{T}}_{w\mathrm{m}}$-3	$\dfrac{K^{\mathrm{E}}_{u\mathrm{m}}\text{-3}}{K^{\mathrm{T}}_{u\mathrm{m}}\text{-3}}$	$\dfrac{K^{\mathrm{E}}_{w\mathrm{m}}\text{-3}}{K^{\mathrm{T}}_{w\mathrm{m}}\text{-3}}$
3.3:1 Bar	33.65	6.6	6.1	5.9	6.19	1.36	1.1	3.56	3.05	0.38	0.36
8.9:1 Bar	21.4	27	~ 16.7	22	~ 22	6.1	5.7	18.78	15.11	0.32	0.38
3:1 Plate	27.2	5.5	6.5	6.3	6.26	0.36	0.59	2.76	3.34	0.13	0.18

TABLE 3. Energy ratios and kurtosis excess factors for the three grids. For the excess factors, the subscript m refers to the maximum value, while the superscripts E and T refer to experiment and estimate (equation (9)) respectively.

defined, such that no v-fluctuations originating from the large-scale side, of magnitude less than $|V_f|$, would be present, because they would not be able to penetrate that deeply into the mixing layer in the given convection time, x/U. If y_f is the distance of the point in question from the geometric centre C, then a crude estimate for V_f would be $\sim -y_f U/x$. As y_f increases, (i.e. proceeding further into the small-scale side) the magnitude of V_f increases and consequently less and less of the large-scale v-p.d.f. is transported across the mixing layer. If u and w were well correlated with v, then it could be assumed that the p.d.f.s of u and w transported by the v-bursts, would be similarly truncated. However, $\overline{uv}$, as discussed above, is quite small and $\overline{vw}$ should be identically zero (a consequence of homogeneity in the z-direction), thus the entire u- and w-p.d.f.s are transported across the mixing layer. Hence, relative to u and w, the v-fluctuations originating from the large-scale side would contribute more to the fourth moment than to the square of the second moment, thereby yielding larger values of K_v than K_u or K_w. Presumably the above argument should hold for the edge of the boundary layer or wake also, i.e. K_v should be greater than K_u or K_w.

For further discussion of the skewness and kurtosis profiles the reader is referred to Pope & Haworth (1987) who have used p.d.f. methods to model our earlier measurements (V&W).

4.4. *The energy budgets*

The equations governing the evolution of $\overline{u^2}$, $\overline{v^2}$, $\overline{w^2}$ and the kinetic energy $k(= \frac{1}{2}\{\overline{u^2}+\overline{v^2}+\overline{w^2}\})$ have been discussed in §2. Figure 14 shows the budgets for the energy components $\overline{u^2}$, $\overline{v^2}$ and $\overline{w^2}$ across the mixing layer, for the 3.3:1 parallel bar grid at $x = 21.2M_2$ ($x = 66.7$ cm) where the mixing layer is well established. From the component energy budgets, the full kinetic energy budget was obtained and this is shown in figure 15. Less complete budget measurements were made for the other two grids and those will not be presented here. The results suggest the same qualitative behaviour as for the 3.3:1 bar grid.

Before describing the form of the budgets in figures 14 and 15 we shall discuss the

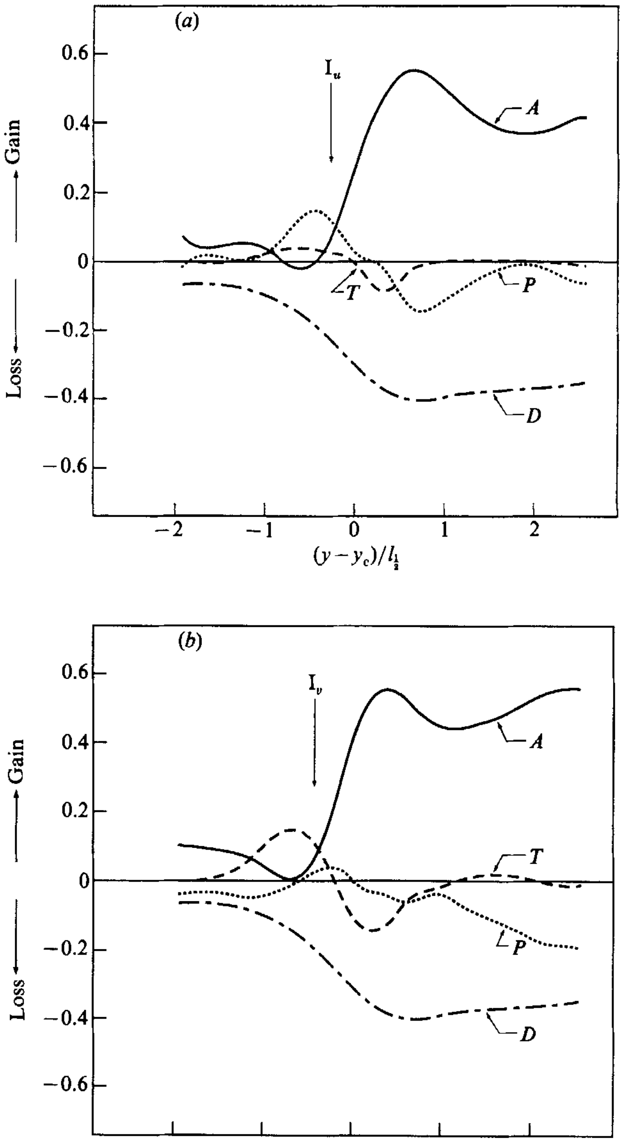

FIGURE 14 (*a*, *b*). For caption see facing page.

way they were deduced from the measurements. In order to determine the longitudinal derivatives, and hence the convection and longitudinal triple-correlation transport terms, two sets of measurements of the second and third moments of u, v and w were made of a distance of approximately one large mesh apart in the longitudinal direction. The locations were $x_1 = 21.2M_2$ (66.7 cm) and $x_2 = 22.1M_2$ (69.5 cm). From these measurements the gradient of $\overline{u^2}$, $\overline{v^2}$, and $\overline{w^2}$ and hence the advection terms $U\partial/\partial x(\overline{u^2})$, $U\partial/\partial x(\overline{v^2})$, and $U\partial/\partial x(\overline{w^2})$ (equation (1)) were calculated using a linear fit. We note that the above procedure would underestimate the gradient at x_1/M_2 and overestimate that at x_2/M_2. Since the budgets were calculated at x_1/M_2, the values obtained above were uniformly increased by 6%.

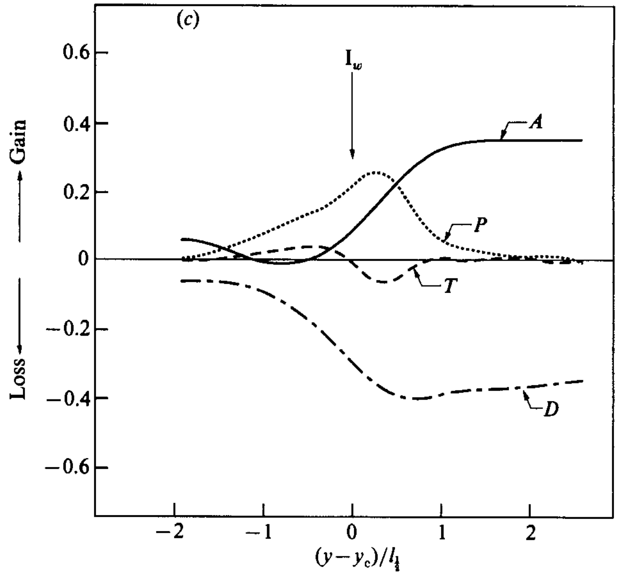

FIGURE 14. Budgets (see equation (1) and §4.4) for the energy components, (*a*) $\overline{u^2}$, (*b*) $\overline{v^2}$ and (*c*) $\overline{w^2}$ across the mixing layer for the 3.3:1 parallel bar grid at $x = 21.2M_2$ (66.7 cm). The ordinate values have been normalized by U^3/x. In (*a*), (*b*) and (*c*), the lateral coordinate has been centred about the geometric centre of the grid and non-dimensionalized by the half-width $l_{\frac{1}{2}}$. The arrows marked I have the same significance as those in figure 8(*a*). The labels indicated in the figure are: *A* ——, normalized advection; *P*······, normalized pressure transport and redistribution; *T* ------, normalized triple-correlation transport; and *D* —·—·—, normalized dissipation $(-2x\epsilon/3U^3)$. The vertical scale has been multiplied by 100.

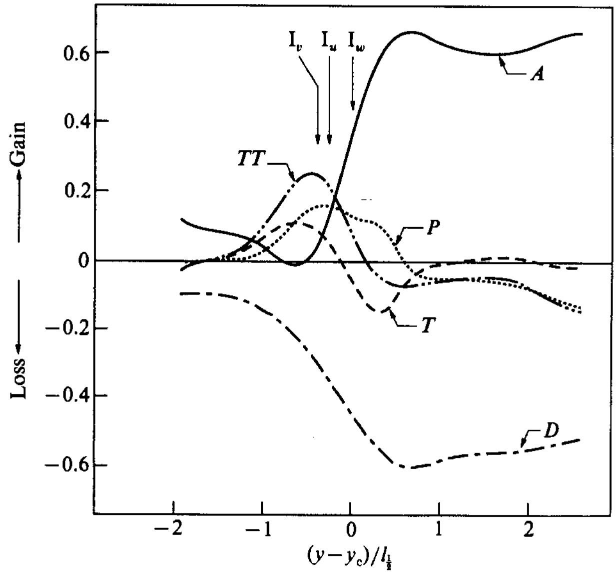

FIGURE 15. The kinetic energy budget (equation (2)) for the 3.3:1 parallel bar grid at $x = 21.2M_2$ (66.7 cm). The abscissa and ordinate have been normalized in the same way as those in figure 14. The arrows marked I have the same meaning as those in figure 8(*a*). The labels are: *A* ——, normalized advection; *P* ······, normalized pressure transport; *T* ------, normalized -triple correlation transport; *D* —·—·—, normalized dissipation; and *TT* —··—··—, normalized total transport (triple correlation plus pressure). The vertical scale has been multipled by 100.

This value was chosen so that the advection terms would match those obtained from the decay laws at the two homogeneous edges of the mixing layer. The dissipation ϵ was estimated from the second moments of the time series $\partial u/\partial t$ and $\partial v/\partial t$, invoking Taylor's frozen-flow hypothesis and local isotropy. The third component $\partial w/\partial t$ was not measured at x_1/M_2; however, measurements further downstream indicate that $\overline{(\partial w/\partial t)^2} = 0.9\,\overline{(\partial v/\partial t)^2}$ across the whole flow (a slight and unexplained departure from that usually found in grid turbulence where $\overline{(\partial w/\partial t)^2} = \overline{(\partial v/\partial t)^2}$). Thus ϵ was determined as equal to $3\nu/U^2(\overline{(\partial u/\partial t)^2}+1.9\overline{(\partial v/\partial t)^2})$. Though the overall contribution to the budget of the downstream transport (triple correlation) terms was negligible, as expected, locally it was found to be as large as 15% of the lateral transport term in the $\overline{u^2}$ and $\overline{v^2}$ budgets. Hence, in these budgets, the downstream transport terms were also included. In the case of $\overline{w^2}$, however, the longitudinal transport term was always less than 5% of the lateral transport term and was therefore dropped from the energy balance. $\partial(\overline{w^2v})/\partial y$ was not measured; however, its value was estimated from $\partial(\overline{u^2v})/\partial y$, assuming that $\overline{w^2v}/[\overline{w^2}\ (\overline{v^2})^{\frac{1}{2}}] = \overline{u^2v}/[\overline{u^2}\ (\overline{v^2})^{\frac{1}{2}}]$. Finally, the pressure terms were obtained as a difference of the terms discussed above, as they could not be measured.

The curves in figures 14 and 15 have been normalized by the mean velocity and the convection time, i.e. by U^3/x. The abscissa has been centred around the geometric centre of the grid and normalized by $l_{\frac{1}{2}}$ obtained from the $\overline{u^2}$ profile. (The inflection points of the variance profiles were not used here for centring as they are different for $\overline{u^2}$, $\overline{v^2}$ and $\overline{w^2}$.)

Figure 14(*a*) shows the energy balance for $\overline{u^2}$ (equation (1*a*)). We note that the dissipation term (and to a lesser extent the advection term) dominates across much of the mixing layer. However, although the respective peak values of the pressure and triple correlation terms are only 35% and 20% of the large-scale dissipation, they are large compared with the dissipation in the low-turbulence side of the layer and there is a region over which the advection is nearly zero, and dissipation is balanced by the pressure and triple-correlation terms alone. For the $\overline{u^2}$ budget, transport due to the pressure–velocity correlation should be negligible (equation (1*a*)) and the pressure term should arise predominantly from the redistribution of the energy components (Tennekes & Lumley 1972). Hence, we would expect it to be positive in the centre of the mixing layer where $\overline{u^2} < \overline{v^2}$ and negative at the large-scale edge, where $\overline{u^2} > \overline{v^2}$ and $\overline{w^2}$ (see figure 8*a*). Figure 14(*a*) shows that this is indeed the case (the negative region in the low-turbulence edge is probably too small in magnitude to detect). The triple-correlation transport term shows a transfer of energy down the gradient, i.e. it is positive on the low-turbulence side and negative on the high-turbulence side.

The budget for $\overline{v^2}$ is shown in figure 14(*b*). The triple-correlation term here is larger than it is in the $\overline{u^2}$ budget, and again there is a region on the low-turbulence side of the mixing layer where it balances dissipation and the advection term is negligible. The triple-correlation term again shows transfer of energy down the gradient. The pressure term in the $\overline{v^2}$ equation consists of both transport and scrambling (redistribution). It shows a fairly large negative region on the high-turbulence side. This behaviour is discussed with reference to the kinetic energy budget below. As in the case of the $\overline{u^2}$ budget discussed above, the advection and dissipation terms dominate over much of the flow.

The $\overline{w^2}$ budget shown in figure 14(*c*) is similar to the $\overline{u^2}$ budget, except for the behaviour of the pressure term. In a similar manner to the $\overline{u^2}$ budget discussed above, the pressure term arises entirely due to redistribution, for the flow is homogeneous in the z-direction, but it is positive throughout the mixing layer (unlike in the $\overline{u^2}$ budget where it has both positive and negative regions) since $\overline{u^2}$ and $\overline{v^2}$ are larger than $\overline{w^2}$ across the whole flow.

Figure 15 shows the total kinetic energy balance. In addition to the curves for advection, dissipation, triple-correlation transport and pressure transport, a fifth curve showing the total transport has been added. As expected from the component energy budgets, the advection and dissipation terms dominate across much of the flow. The behaviour of the pressure transport term is interesting; it has a negative region that extends well into the high-turbulence side of the flow and it is positive in most of the mixing layer (presumably, close to the wall the pressure term should go to zero; the fact that it does not is probably due to interference from the boundary layer). There is a region near the geometric centre of the grid where the pressure and triple correlation terms oppose each other. This suggests that energy transfer across the mixing layer takes place due to two distinct mechanisms. The triple-correlation term is involved in essentially a gradient-diffusion-like mechanism and is hence active in the central region of the mixing layer where strong gradients are present. The pressure term, on the other hand, transfers energy from the entire large-scale side of the flow (including the nearly homogeneous region), to the central and small-scale regions of the mixing layer. The total transport curve therefore shows energy transfer from the entire region to the right of the geometric centre, to the region to the left of it.

Finally, some consistency checks were made on the transport terms. The lateral triple-correlation transport term and the lateral pressure transport term, should integrate to zero across the mixing layer as the flow is homogeneous at $y \rightarrow \pm \infty$. The ratio of the total integral to the integral over the positive region alone was used to test the accuracy of the measurements. The error in the triple-correlation transport term was found to be extremely low, approximately 0.6 %. The integral of the total pressure term, however, showed a residue of about 25 %. This is partly due to the measurements not extending far enough into the large-scale side, thereby truncating the domain of integration and partly due to the downstream transport component $(\partial(\overline{pu^2})/\partial x)$ being included in the integrand. The downstream transport term need not integrate to zero. Finally, error is also introduced because the pressure term is deduced from a difference of the other terms in the budget.

4.5. *The lengthscales and spectra*

As seen from the discussion of the various velocity moments above, the u-, v- and w-fluctuations behave differently from each other in the mixing layer. Hence we could expect different characteristic lengthscales for u, v and w as well. In order to study the length-scale of each component separately we define the following:

$$l_{11} \equiv \frac{(\overline{u^2})^{\frac{3}{2}}}{6\nu \overline{\dfrac{\partial u}{\partial x}\dfrac{\partial u}{\partial x}}}, \tag{11a}$$

$$l_{22} \equiv \frac{(\overline{v^2})^{\frac{3}{2}}}{6\nu \overline{\dfrac{\partial v}{\partial x}\dfrac{\partial v}{\partial x}}}, \tag{11b}$$

and

$$l_{33} \equiv \frac{(\overline{w^2})^{\frac{3}{2}}}{6\nu \overline{\dfrac{\partial w}{\partial x}\dfrac{\partial w}{\partial x}}}. \tag{11c}$$

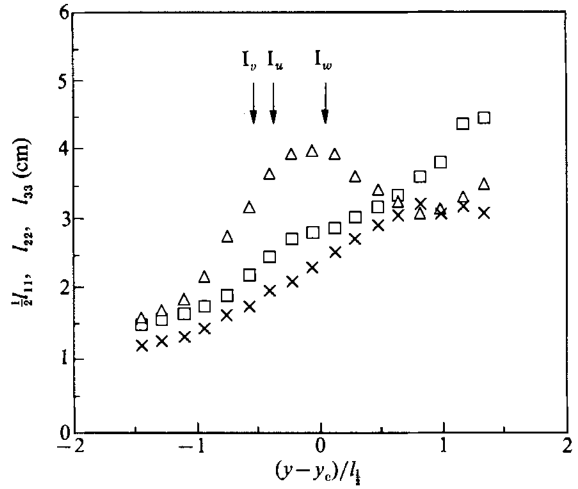

FIGURE 16. Profiles of the component length scales $\frac{1}{2}l_{11}$, l_{22} and l_{33} (equation (11)) for the 3.3:1 bar grid at $x = 49.5M_2$ (156 cm). The lateral coordinate has been centred about the geometric centre of the grid and normalized by the half-width $l_{\frac{1}{2}}$. The arrows marked I have the same significance as those in figure 8(*a*). □, $\frac{1}{2}l_{11}$, △, l_{22}; ×, l_{33}.

These lengthscales have been defined in a manner analogous to that used for the integral scale in homogeneous turbulence $l = k^{\frac{3}{2}}/\epsilon$. Here, however, both the kinetic energy and dissipation have been partitioned into their respective components. Similar definitions for the Taylor microscales

$$\left[\left(\overline{u^2}\bigg/\overline{\frac{\partial u}{\partial x}\frac{\partial u}{\partial x}}\right)^{\frac{1}{2}},\ \left(\overline{v^2}\bigg/\overline{\frac{\partial v}{\partial x}\frac{\partial v}{\partial x}}\right)^{\frac{1}{2}}\right]$$

have been used (see for example Bradshaw 1971) but we are unaware of previous use of the above-defined lengthscales. We shall show below (figure 19 and related discussion) that the lengthscales defined by (11) are in good agreement with those derived from the spectra.

Figure 16 shows the variation of l_{11}, l_{22} and l_{33} across the mixing layer for the 3.3:1 bar grid at $x = 49.5M_2$ (156 cm). Because of the manner in which the dissipation has been partitioned, l_{11} would be twice as large as l_{22} and l_{33} even in homogeneous isotropic turbulence. It has, therefore, been reduced by a factor of 2 before being compared with l_{22} and l_{33}. The arrows marked I have the same meaning as those in figure 8. There is a monotonic increase of l_{11} and l_{33} from small values in the low-turbulence region to large values in the high-turbulence region. On the other hand, though l_{22} is nearly equal to l_{33} at the two homogeneous ends of the mixing layer, it differs sharply from it in the central region. Proceeding from the high-turbulence region, l_{22} first dips down slightly and then increases to a value 20% larger than that in the large-scale homogeneous region, before dropping steeply to the value in the low-turbulence homogeneous region.

This behaviour may again be explained by the presence of the cutoff velocity V_f (see §4.3) for the large-scale bursts penetrating the small scale-side of the mixing layer. The more deeply a large-scale event penetrates the mixing layer, the larger the magnitude of its v-component must be. Since large velocity fluctuations are more likely to be associated with large lengthscales, the large-scale v-fluctuations preferentially transport themselves across the mixing layer. Furthermore, the fractional contribution of each large-scale burst to the local lengthscale progressively increases as y decreases since the local turbulence intensity decreases. Hence we see a region in the mixing layer where l_{22} is larger than its value in the large-scale homogeneous region. As y decreases further, however, the large-scale bursts become so infrequent that the small-scale fluctuations dominate, causing the lengthscale to decrease. However, since u and w are not well correlated with v the full spectrum of these two components is transported across the mixing layer in a similar way to the velocity p.d.f. as discussed in §4.3. Hence l_{11} and l_{33} vary monotonically across the mixing layer.

Figure 17 shows a log–log plot of the one-dimensional spectra of u- and v-fluctuations, measured at $x = 49.5M_2$ (156 cm) for the 3.3:1 bar grid. The uppermost spectrum in each of figures 17(*a*) and 17(*b*) was obtained from the large-scale homogeneous region of the mixing layer while the lowest was obtained from the small-scale homogeneous region. The longitudinal ($F_{11}(\kappa_1)$) and transverse ($F_{22}(\kappa_1)$) spectra were calculated from the u- and v-time series respectively, using Taylor's hypothesis. The spectra shown are one sided, hence,

$$\int_0^\infty F_{11}(\kappa_1)\,\mathrm{d}\kappa_1 = \overline{u^2}, \quad \int_0^\infty F_{22}(\kappa_1)\,\mathrm{d}\kappa_1 = \overline{v^2}.$$

The longitudinal spectra (figure 17*a*) are similar in shape across the whole mixing layer. At the large-scale homogeneous end of the mixing layer, the integral lengthscale l_2, is larger, while the Kolmogorov lengthscale η_2, is smaller (owing to the larger dissipation rate ϵ_2), than the corresponding values (l_1 and η_1) at the low-turbulence region (see table 1). Hence, we would expect to see a larger separation of scales (i.e. a wider spectrum) in the high-turbulence region and this is observed in figure 17(*a*).

The behaviour of the transverse spectra (figure 17*b*) is more interesting. On the large-scale side of the mixing layer, inclusive of the homogeneous region, the spectra show a region of power-law decay with wavenumber (indicated by the straight lines adjacent to the spectra). This behaviour is at variance with what is normally observed in grid turbulence and is discussed below. Within the mixing layer the low-wavenumber region of the spectrum is enhanced due to the same mechanism that caused the increase in l_{22} (figure 16).

The behaviour of the other one-dimensional spectrum, $F_{33}(\kappa_1)$ (not shown), across the mixing layer is very much like that of $F_{11}(\kappa_1)$. Here too, the spectra are similar in shape throughout the flow and show a large separation of scales in the high-turbulence region and a small separation of scales in the low-turbulence region.

Figure 18 shows the plots of $\kappa_1 F_{11}(\kappa_1)/\overline{u^2}$ and $\kappa_1 F_{22}(\kappa_1)/\overline{v^2}$ *vs.* log(κ_1) obtained from the raw spectra shown in figure 17. A ninth-order polynomial was fit to the raw spectra in log–log space prior to the calculation of the energy spectra $\kappa_1 F_{11}(\kappa_1)/\overline{u^2}$ and $\kappa_1 F_{22}(\kappa_1)/\overline{v^2}$. The curves of $\kappa_1 F_{11}(\kappa_1)/\overline{u^2}$ are similar in shape throughout the mixing layer and the peak shifts into lower wavenumbers as y increases (i.e. proceeding from the low-turbulence region to the high-turbulence region). On the other hand, proceeding from the high-turbulence region to the low, the peak of $\kappa_1 F_{22}(\kappa_1)/\overline{v^2}$ is seen to first shift slightly towards lower wavenumbers before increasing to the value attained in the low-turbulence homogeneous region. The reciprocal of the peak wavenumber may be viewed as an approximate measure of the integral scale. Figure 19 shows the variation of the reciprocals of the peak wavenumbers of $\kappa_1 F_{11}(\kappa_1)$, $\kappa_1 F_{22}(\kappa_1)$ and $\kappa_1 F_{33}(\kappa_1)$, denoted by l'_{11}, l'_{22} and l'_{33} respectively, across the mixing layer at $x = 49.5M_2$ for the 3.3:1 bar grid. (Just like l_{11} in figure 16, l'_{11} has been reduced by

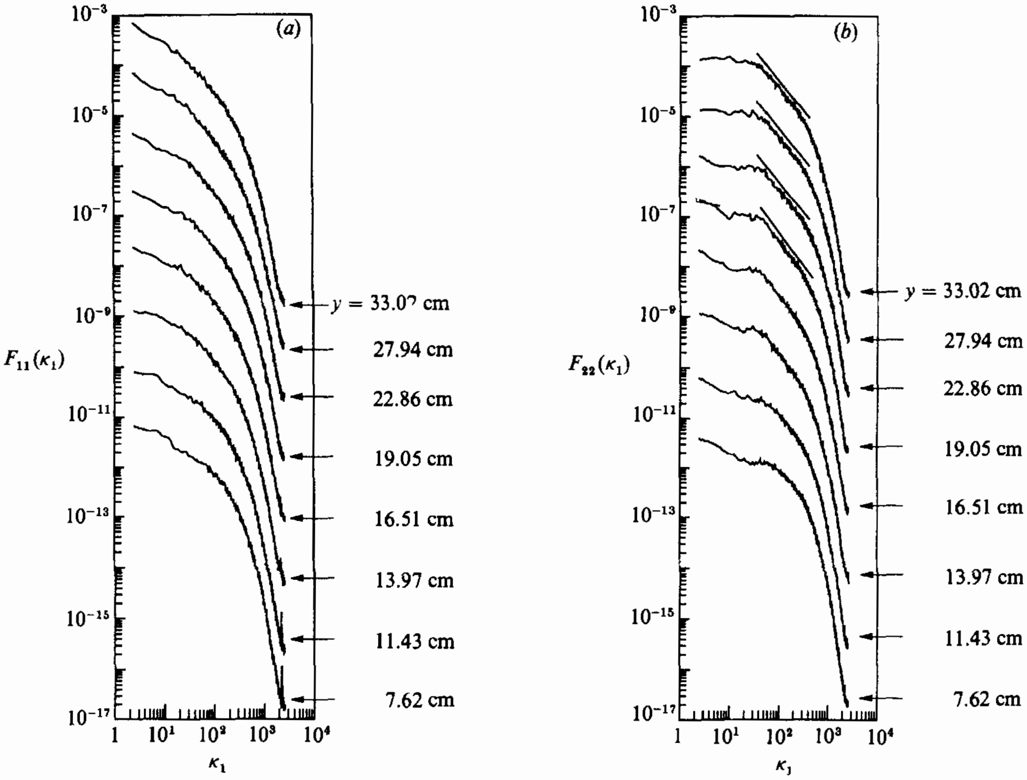

FIGURE 17. One-dimensional spectra at various lateral positions (indicated on the figure) in the mixing layer for the 3.3:1 parallel bar grid at $x = 49.5M_2$ (156 cm). The longitudinal spectra $F_{11}(\kappa_1)$ are shown in (*a*) and the transverse spectra $F_{22}(\kappa_1)$ are shown in (*b*). To permit comparison, each spectrum has been shifted down a decade with respect to the one above it. We note that the inflection point I_u occurs at $y = 12.59$ cm, I_v occurs at $y = 15.0$ cm and the geometric centre of the grid is at $y = 18.2$ cm.

a factor of 2.) We note that the qualitative behaviour is very similar to that shown in figure 16.

Figure 20 shows the profiles of l'_{11} and l'_{22} for the 8.9:1 bar grid at $x = 21.4M_2$ (91 cm). This figure clearly indicates the dominance of the large scale over most of the flow. The transition from the large-scale value to the small-scale value for both l'_{11} and l'_{22} occurs well to the left of the respective inflexion points and is particularly sharp for l'_{22}. This should be compared with the behaviour for the 3.3:1 bar grid (figures 16 and 19) for which the transition from large scale to small scale begins slightly to the right of the inflexion points, and for which the change is more gradual because of the interaction of the two lengthscales.

Figure 20 suggests, then, that the 8.9:1 grid is close to the situation of turbulence spreading into an irrotational region, a case of significant theoretical interest (Phillips 1972). For the mixing layer described here the ratios of mean-squared vorticity $[(\overline{u_2^2}/\lambda_2^2)/(\overline{u_1^2}/\lambda_1^2)]$ and turbulence energy on either side of the mixing layer both vary as $(M_2/M_1)^n$, where n, the turbulence energy decay power-law exponent, is approximately 1.3 (table 1). Thus as M_2/M_1 is made large the relative contributions of turbulence energy and vorticity on the small-scale side may be made as small as desired. Moreover the further we proceed downstream the smaller the turbulence

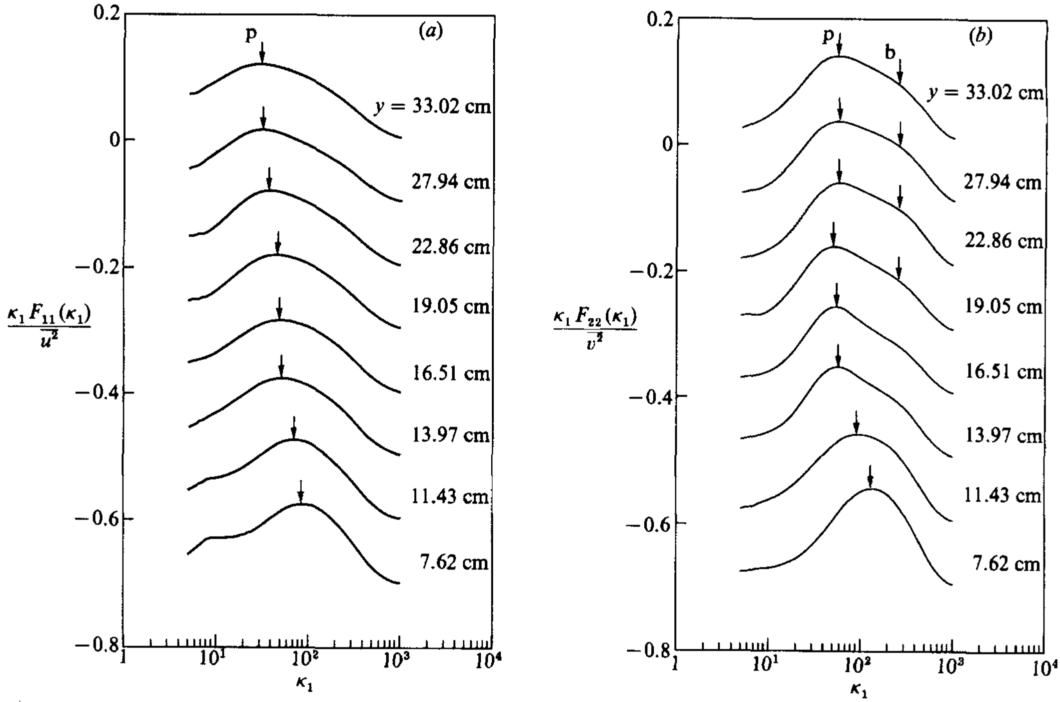

FIGURE 18. Normalized one-dimensional (*a*) longitudinal energy spectra, $\kappa_1 F_{11}(\kappa_1)/\overline{u^2}$ and (*b*) transverse energy spectra, $\kappa_1 F_{11}(\kappa_1)/\overline{v^2}$ obtained from the spectra shown in figure 17. Each curve has been shifted down by a value of 0.1 with respect to the one above it. The arrows marked p indicate the locations of the peaks of these curves while the arrows marked b (*b* only) indicate the approximate location of the bump in the spectra.

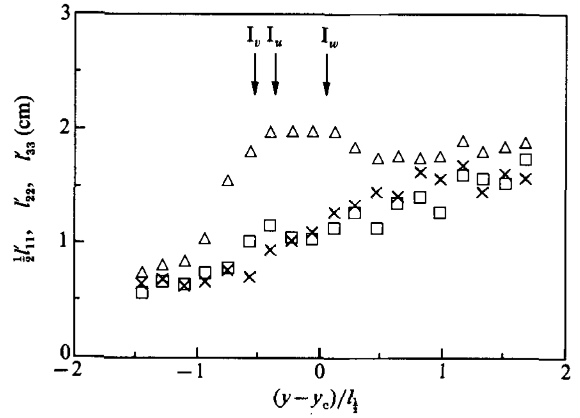

FIGURE 19. Profiles of the component lengthscales $\frac{1}{2}l'_{11}$, l'_{22}, and l'_{33} (§4.5) for the 3.3:1 bar grid at $x = 49.5M_2$ (156 cm). The normalization of the abscissa is the same as that in figure 16 and the arrows have the same significance as those in figure 8(*a*). □, $\frac{1}{2}l'_{11}$; △, l'_{22}; ×, l'_{33}.

Reynolds numbers become (table 1). Thus the Reynolds number on the small-scale side may be made to approach a value so small that viscous forces dominate this entire region (the final period of decay, Batchelor 1953) while the Reynolds number on the large-scale side is still at a significantly high value. For the 8.9:1 grid the mean-squared vorticity ratio is 26, the turbulence energy ratio is 22 and the

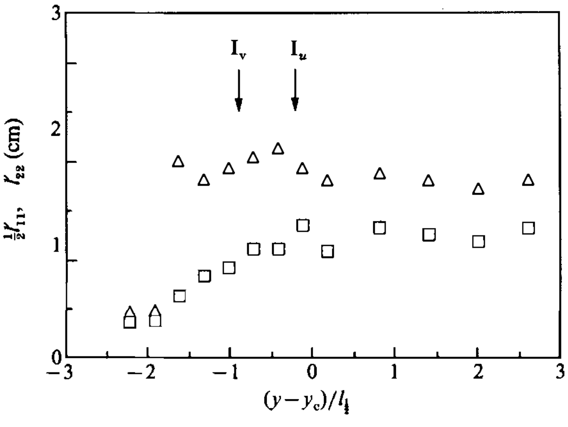

FIGURE 20. Profiles of the component length scales $\frac{1}{2}l'_{11}$ and l'_{22} (§4.5) for the 8.9:1 bar grid at $x = 21.4M_2$ (91 cm). The normalization of the abscissa is the same as that in figure 16 and the arrows have the same significance as those in figure 8(*b*). □, $\frac{1}{2}l'_{11}$, △, l'_{22}.

Reynolds numbers based on the Taylor scale are $R_{\lambda_1} = 18.2$ and $R_{\lambda_2} = 96.5$ (table 1). While these values clearly indicate that we are not at the irrotational limit on the small-scale side of the mixing layer, figure 20 when contrasted with figure 19, does suggest that the layer is dominated by the large scale and that if M_2/M_1 were increased further there would be little change in the qualitative picture.

In the discussion of figure 17 above it was noted that some of the *v*-spectra showed a region of power-law decay with κ_1. The corresponding curves of $\kappa_1 F_{22}(\kappa_1)/\overline{v^2}$ show the presence of a small bump in this region to the right of the peaks. While the magnitude of the bump is too small to significantly affect the dynamics of the flow, its presence is curious. Figure 21 shows a comparison of the location of the peak of $\kappa_1 F_{22}(\kappa_1)$ and the location of the bump. We see that the bump occurs at a wavenumber much larger than the peak of the energy spectrum in both the low- and high-turbulence homogeneous regions, hence it cannot be an artifact of the mixing layer. The only other source of small-scale fluctuations is the blocks (see §3.1 for details) glued onto the large bars. The block width is smaller than the small bar width for the 3.3:1 grid (see figure 2) and this is consistent with the larger wavenumber of the bump. This conjecture is confirmed by a study of the other two grids (not shown); the bump does not appear in the energy spectra of the 3:1 perforated plate since blocks were not used for this grid, while for the 8.9:1 bar grid, the bump occurs at the same wavenumber as the peak of $\kappa_1 F_{22}(\kappa_1)$ in the low-turbulence homogeneous region, since the block width is the same as the small bar width here (figure 2).

Hence, the blocks give rise to a spectral disturbance similar in some respects to the one caused by the zither in the experiments of Kellogg & Corrsin (1980) and Itsweire & Van Atta (1984). However, while the zither primarily perturbs the *u*-spectrum, here it is the *v*-spectrum that is affected. A comparison of the turbulence kinetic energy levels in the large-scale homogeneous region, at the same *x*/*M*, with and without the blocks, indicates that even when the mean velocity is maintained at the same value, the energy is about 30% lower when blocks are present. The decay exponent is also found to increase from approximately 1.1 to 1.3 when blocks are added. Hence, the presence of small-scale fluctuations arising from the blocks causes a more rapid decay of the turbulence in the large-scale homogeneous region. This observation is consistent with the zither experiments (Kellog & Corrsin 1980; and

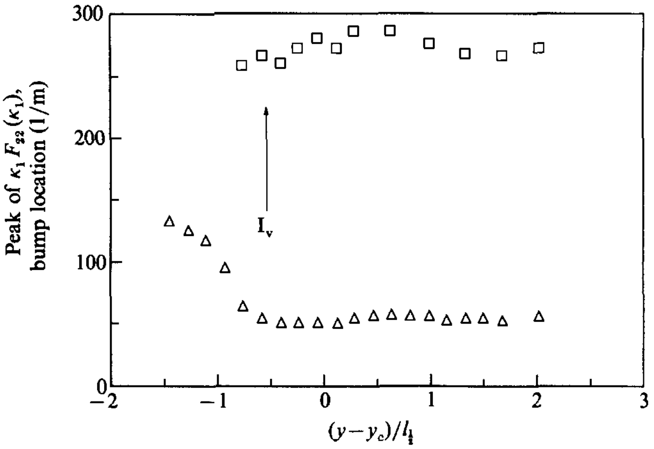

FIGURE 21. Comparison of the location of the peak of the one-dimensional transverse energy spectra (figure 18*b*), with the location of the bump on these spectra. The normalization of the abscissa is the same as that in figure 16. △, location of the peak of $\kappa_1 F_{22}(\kappa_1)$; □, location of the bump.

Itsweire & Van Atta 1984), wherein the turbulence was found to decay more rapidly with the zither present; however, the decay laws were not documented in those studies. The numerical studies of Orlandi & Grocco (1985) also show the same behaviour, though it should be noted that the Reynolds number was much larger in their work.

5. Conclusions

The turbulence mixing layer is remarkably rich and complex for a flow without shear in decaying grid turbulence. In this experiment we have studied its dependence on initial conditions and have documented single point statistics and some spectral quantities of the data. There are many other aspects of that warrant study. These include flow visualization, scalar dispersion, conditional sampling and the study of the large-scale structure. In this regard this study is preliminary (and somewhat classical) but we feel it is important to investigate the overall energetics of the turbulence before considering the more subtle aspects.

We shall now summarize our main findings.

There appear to be two asymptotic states of the shearless mixing layer. The first is described by Gilbert (1980). Here the lengthscale ratio is small (in his case 1.4), the velocity variance follows the form of an error function and the velocity fluctuations are Gaussian ($S = 0, K = 3$). The flow can be considered essentially of one scale with a region of large variance diffusing into a region of lower variance. The other asymptotic state is that of our large lengthscale ratio (8.9:1 parallel bar grid). Here the flow appears to be dominated by the large-scale side of the flow since the energy on the small-scale side is too weak to have any effect (the turbulence energy ratio is 22:1, table 3). However, unlike the case of Gilbert, here the flow is highly intermittent and the velocity statistics are non-Gaussian (figures 11*b* and 12*b*) although the velocity variance profiles are close in form to an error function (figure 9*b*). This is the case closest to turbulence spreading into an irrotational flow (§4.5). For the in-between cases (the perforated plate and the 3.3:1 parallel bar grid) the lengthscale ratio (2.4:1 and 2.2:1 respectively) is such that both scales play an important role in the energetics (§4.5). Here the velocity fluctuations are non-Gaussian (as for the 8.9:1 grid) but unlike the two asymptotic cases the velocity variance does not follow an error function (figure 9*a* and 9*c*).

The perforated plate yielded qualitatively similar results to the bar grid for the cases in which their mesh ratios were similar (§§4.2 and 4.3). However, while the bar grid approached self-similarity with downstream distance, we were unable to measure sufficiently far downstream to determine whether the perforated plate would reach self-similarity (figure 10*a*). For both these grids the integral timescale ratio was approximately constant across the entire flow (figure 10*b*).

The energy budget, investigated in detail only for the 3.3:1 bar grid, shows the importance of the triple-moment transport terms in affecting the spreading of the mixing layer. These terms become dominant on the small-scale side of the layer; on the large-scale side they are swamped by advection and dissipation (figures 14 and 15). (One could conjecture a situation in which there was no decay of turbulence on either side of the layer and thus the longitudinal advection term would be zero.)

Finally, we have emphasized that in this flow spreading is affected by turbulent diffusion *and* by the intermittent penetration of one field into the other. In our experiment both effects were important (figure 13) whereas in the earlier work of Gilbert (1980) no intermittency was observed and thus diffusion was the sole spreading agent.

We wish to thank Mr E. P. Jordan for his enthusiastic technical assistance, Ms E. Ikeda for her help with the construction of the grids and with measurements and Professor S. B. Pope and Dr W. R. C.Phillips for their comments on the final form of this paper. This work was supported by grants from the Department of Energy (Basic Energy Sciences, DE-FG-02-88ER13929) and the US National Science Foundation (Atmospheric Science, ATM-8412558).

REFERENCES

BATCHELOR, G. K. 1953 *The Theory of Homogeneous Turbulence.* Cambridge University Press.

BRADSHAW, P. 1971 *An Introduction to Turbulence and its Measurement.* Pergamon.

BREIDENTHAL, R. E. 1981 Structure in turbulent mixing layers and wakes using a chemical reaction. *J. Fluid Mech.* **109**, 1–24.

CHAMPAGNE, F. H. & SLEICHER, C. A. 1967 Turbulence measurements with inclined hot-wires. Part 2. Hot-wire response equations. *J. Fluid Mech.* **28**, 177–182.

CHAMPAGNE, F. H., SLEICHER, C. A. & WEHRMAN, O. H. 1967 Turbulence measurements with inclined hot-wires. Part 1. Heat transfer experiments with inclined hot-wire. *J. Fluid Mech.* **28**, 153–176.

COMTE-BELLOT, G. & CORRSIN, S. 1966 The use of a contraction to improve the isotropy of grid generated turbulence. *J. Fluid Mech.* **25**, 657–682.

CORRSIN, S. 1950 Hypothesis for skewness of the probability density of the lateral velocity fluctuations in turbulent shear flow. *J. Aeronaut. Sci.*, **17**, 396–398.

GILBERT, B. 1976 An experimental investigation of turbulent mixing of fluids with different dynamically significant scales. Ph.D. thesis, University of Illinois at Chicago circle.

GILBERT, B. 1980 Diffusion mixing in grid turbulence without mean shear. *J. Fluid Mech.* **100**, 349–365.

HERRING, J. R. 1985 Some contributions of two-point closure to turbulence. In *Frontiers in Fluid Mechanics* (ed. S. H. Davis & J. L. Lumley), pp. 68–87. Springer.

HINZE, J. O. 1975 *Turbulence.* McGraw-Hill.

ITSWEIRE, E. C. & VAN ATTA, C. W. 1984 An experimental study of the response of nearly isotropic turbulence to a spectrally local disturbance. *J. Fluid Mech.* **145**, 423–445.

KELLOG, R. M. & CORRSIN, S. 1980 Evolution of a spectrally local disturbance in grid-generated, nearly isotropic turbulence. *J. Fluid Mech.* **96**, 641–669.

MAXEY, M. R. 1987 The velocity skewness measured in grid turbulence. *Phys. Fluids* **30**, 935–938.

ORLANDI, P. & CROCCO, L. 1985 Interaction between isotropic turbulent fields of different scales. *Fifth Symposium on Turbulent Shear Flows, Cornell University*, pp. 2.19–2.25.

PHILLIPS, O. M. 1972 The entrainment interface. *J. Fluid Mech.* **51**, 97–118.

POPE, S. B. & HAWORTH, D. C. 1987 The mixing layer between turbulent fields of different scales. In *Turbulent Shear Flows 5* (ed. L. T. S. Bradbury *et al.*), pp. 44–53. Springer.

RODI, W. & SCHEUERER, G. 1985 Calculation of turbulent boundary layers under the effect of free stream turbulence. *Fifth Symposium on Turbulent Shear Flows, Cornell University*, pp. 15.1–15.5.

SIRIVAT, A. & WARHAFT, Z. 1983 The effect of a passive cross-stream temperature gradient on the evolution of temperature variance and heat flux in grid turbulence. *J. Fluid Mech.* **128**, 232–346.

TENNEKES, M. & LUMLEY, J. L. 1972 *A First Course in Turbulence.* MIT Press.

TOWNSEND, A. A. 1976 *The structure of turbulent shear flows.* Cambridge University Press.

VEERAVALLI, S. & WARHAFT, Z. 1987 The interaction of two distinct turbulent velocity scales in the absence of mean shear. In *Turbulent Shear Flows 5* (ed. L. T. S. Bradbury *et al.*), pp. 31–43. Springer (referred to as V&W).

WARHAFT, Z. 1981 The use of dual heat injection to infer scalar covariance decay in grid turbulence. *J. Fluid Mech.* **104**, 93–109.

WARHAFT, Z. 1984 The interference of thermal fields from line sources in grid turbulence. *J. Fluid Mech.* **144**, 363–387.